Biofabrication

International Society for Biofabrication

PURPOSE-LED PUBLISHING™

Biofabrication of high aspect ratio, flexible, and bioconductive micropillar arrays of PEDOT:PSS composite for 3D printed bioelectronics

To cite this article before publication: Miriam Seiti *et al* 2025 *Biofabrication* in press https://doi.org/10.1088/1758-5090/ae16d8

Title Biofabrication of High Aspect Ratio, Flexible, and Bioconductive Micropillar Arrays of PEDOT:PSS Composite for 3D Printed Bioelectronics

Miriam Seiti[a,b], Rosalba Monica Ferraro[c], Eleonora Ferraris[a]*

M. S. Author 1, E.F. Author 3

MaPS, Department of Mechanical Engineering, KU Leuven, Sint Katelijne Waver, 2860, Belgium
E-mail: miriam.seiti@kuleuven.be

E-mail: miriam.seiti@unibs.it

M. S. Author 1

Department of Mechanical and Industrial Engineering, University of Brescia, Brescia, 25123, Italy

R.M.F. Author 2

Department of Molecular and Translational Medicine, "Angelo Nocivelli" Institute for Molecular Medicine, University of Brescia, ASST Spedali Civili, Brescia, 25123, Italy

Keywords: PEDOT:PSS, bioelectronics, 3D aerosol jet printing, process analysis, microfabrication; neural cells

Abstract. The next generation of 3D micro-additive manufacturing (AM) bioelectronics requires inks that simultaneously combine high electrical conductivity, biocompatibility, electrochemical stability, and compatibility with 3D processing. However, most existing inks fail to meet all these criteria, with processability and repeatability remaining major bottlenecks. This challenge is particularly serious in printed electronics technologies, such as Aerosol Jet® Printing (AJ®P), for which commercially available formulations tailored to specific applications are still scarce. Here, we present a novel Poly(3,4-ethylenedioxythiophene) polystyrene sulfonate (PEDOT:PSS)-based ink incorporating polyethylene glycol, ethylene glycol, and carboxymethyl cellulose to obtain a composite that fulfils all requirements, being conductive, processible by AJ ® P and biocompatible. The formulation exhibits high conductivity (σ = 495.29 $S \cdot cm^{-1}$), electrochemical stability, and biocompatibility with both human fibroblasts and iPSC-

derived neural stem cells. Its low viscosity (μ = 7.93 mPa·s) enables precise and repeatable AJ®P fabrication while supporting controlled, high-resolution 2D patterning and 3D microfabrication with aspect ratios up to 9. Dense or hollow microarrays of 24 flexible pillars (diameter ≥ 35 μm; elastic modulus = 3.1 × 10^6 Pa per pillar) can be fabricated within 10 minutes, without masks or supporting materials. This work focuses on the material and process optimization study of a customizable bioink for AJ®P in 3D micro-AM bioelectronics, with potential applications in 3D microelectrode arrays, biosensors, tissue engineering.

1. Introduction

Bioelectronics focuses on the integration and incorporation of electronic components with biological systems and processes. Bioelectronics devices are increasingly used for sensing or stimulation of biological interfaces or as signal transduction. Among bioelectronic units, three-dimensional (3D) periodic micro- or meso-structures at high aspect ratios (ARs) have garnered considerable being suitable in cell guidance, interfacing biosensors, 3D electroactive interfaces, and microelectrode arrays (MEAs) due to their high surface area, mechanical compliance and improved tissue-interface interaction.[1,2] Among the various bioelectronic microarchitectures, micropillars have been employed as 3D electrodes to increase the sensing surface area in bioelectronic interfaces, which in turn reduces electrode impedance and improves the signal-to-noise ratio, compared to planar electrodes.[3] For instance, ARs polythiopene-based pillars (height ~ 6.4 μm, diameter ~ 2.3 μm) have been exploited for soft 3D cultures of primary neurons,[4] microtubes (up to 130 μm in height, AR of 16) to direct hippocampal neuronal growth through multi-photon polymerization,[5] while microgroove and nanopore patterns (groove ~ 1.5 μm, pores diameter ~ 10 nm) have been employed to differentiate human neural stem cells (NSCs) into neurons.[6]

However, the development of such bioarchitectures frequently faces challenges as high prototyping costs, sensor reliability, reproducibility issues, short lifespans, and weak mechanical properties in response to deformations and fractures. Additive manufacturing (AM) applied for bioelectronics offers significant potential for developing custom-made active and passive components that interact with biological (living) systems, that are essential for the future of personalized medicine. This specialized and novel topic, within the broader multidisciplinary field of printed electronics (PE), has been gaining increasing attention, especially over the last decade. PE technologies, such as roll-to-roll, screen printing, and jet-

based printing, are indeed capable of manufacturing thin, light, flexible, wearable electronics, (bio)sensors and patches at reduced prototyping costs and shorten time to market, compared to conventional lithography-based processes.[7–9] In digital PE, functional materials are selectively deposited onto a surface in a defined digital pattern to form bioelectronic components and integrated circuits (IC). So far, Zips et al. fabricated a functional 3D printed microelectrode array (MEA) by means of Aerosol Jet® Printing (AJ®P), to perform electrophysiological tests on neuro-spheroids and cerebral organoids for 6 weeks long,[10] while Kundu et al. proposed a 3D MEA with 3D printed micro towers and conductive traces by stereolithography for the recording and stimulation of dorsal root ganglion (DRG) cells.[11]

Nevertheless, PE is relatively recent and often shows limited performance compared to silicon ICs, especially in bioelectronics. This is firstly related to the scarcity of biocompatible, stable, and electroactive biomaterials processable into 3D bioelectronics microfeatures. Secondly, there are currently only a few suitable PE technologies that can be optimized towards the reliable and versatile fabrication of 2D or 3D structures at the micro- or meso-scale, and which are also compatible with bioelectronic materials. These technologies primarily include inkjet printing (IJP), screen printing and AJ®P. IJP has been extensively used in PE to deposit picolitre-sized droplets (viscosity 1-30 cPs) at high repetition rates (up to 100 kHz) and fixed offsets of usually 1 mm, with resolutions ≥ 40 µm.[12] Conductive materials (Ag, Au, Pt, Cu, Ni, poly(3,4-ethylenedioxythiophene) polystyrene sulfonate (PEDOT:PSS), polypyrrole (ppy), carbon-based inks) and dielectrics (SU-8, polyimide) have been widely IJ printed.[13] IJP has also been explored for bioelectronic applications, including Au electrode arrays,[14] cell-interfacing electrodes[15], and biosensors[16].[17] However, it is limited to printing 2D inks specifically formulated for IJP and at a fixed offset, restricting its ability to create 3D bioelectronic microstructures. Screen printing is instead an industrialized PE process for large area electronics, in which a paste-like ink of 1000-25000 cPs (Ag, Cu, carbon-based, dielectrics) is deposited on a mesh with a stencil, with resolutions < 70 µm.[18] Screen printing has been also exploited in bioelectronics, especially in the fabrication of electrochemical biosensors,[19] including glucose sensors,[20] a bioelectronic tongue and bio-optoelectronics.[21] However, screen-printing makes use of masks and has limited resolution, which diminish its versatility for printing both 2D and 3D microstructures.

In this context, AJ®P offers interesting opportunities for bioelectronics. AJ®P is a direct writing technique, classified as maskless or digital PE technology, which deposits functional aerosolized (nano-)inks on rigid or flexible *free-form* substrates at a variable stand-off distance of [1-5] mm, with thin layer thicknesses of ~ 100 nm and trace widths down to 15 µm.[22]

Originally developed by ©Optomec (Albuquerque, USA) for planar electronic circuitry (as antennas,[23] transistors,[24] or sensors,[25,26]), few case studies have recently reported the use of AJ®P as 3D printing technique (3D-AJ®P). Especially when using a 3D layer-by-layer (LBL) approach, 3D-AJ®P allows the production as vertically aligned, multi-layered arrays. Few case studies have been reported in the literature, including silver nanoparticle (AgNPs)-based lattice structures and micropillars with aspect ratios (ARs) ~ 20, fabricated in less than 1.5 h,[27] indium tin oxide (ITO) NPs pillar arrays with ARs up to ~ 30,[28] and recently, as reported by the same authors, AuNPs pillars with an AR ≤ 9 [29] and polymeric-based inks with ARs from 2.5 to 4.5.[30] Therefore, 3D-AJ®P, offers significant potential for the rapid and digital production of bioelectronics interfaces, however the process repeatability remains a technological constraint not yet been fully examined and limits a wider use within the scientific and industrial community. Furthermore, the biocompatibility of these structures is a critical concern, as the majority of them are produced using commercial AJ®P inks, which are primarily derived from optimised ink-jet inks initially designed for PE rather than bioelectronics, with Ag-based inks being the standard. Ink formulations indeed frequently contain cytotoxic loading agents or co-solvents (such as oils, xylenes, glycols, and alcohols), which typically result in oxidative stress and cellular apoptosis.[31] Among glycols, diethylene glycol (DEG) is commonly used in commercial PEDOT:PSS inks to enhance electrical conductivity; however, its low volatility and high cytotoxicity can lead to residual solvent in printed structures, posing risks for cellular applications.[32] In contrast, ethylene glycol (EG) has a higher vapor pressure and lower cytotoxicity, allowing more efficient removal during fabrication while retaining its function as a secondary dopant to improve conductivity, printability, and better biocompatibility. This highlights the critical importance of selecting appropriate solvent systems for bioconductive inks.

This scenario presents numerous challenges from material science, technological, and bioelectronic perspectives, resulting in a multi-objective and multidisciplinary problem. Consequently, the development of custom-made inks that are conductive, biocompatible, electrochemically stable, and possess mechanical properties akin to the target tissue interface is essential. In addition to these primary features, this biomaterial must also be processable, such as an ink through AM. In this study, we therefore propose the development of an ink formulation which meets all necessary criteria for being identified as a bioelectronic ink and that can be processable with an AM technology, as AJ®P, and which formulation can also be optimized for other AM techniques, such as IJP and direct ink writing, and extended to spin coating, drop casting, or similar deposition technologies. The conductive polymer PEDOT:PSS

is here chosen as main loading content, being a well-known synthetic, biocompatible organic electrode material with π-conjugated backbones,[33] a mixed ionic-electronic conductivity, good processability, electrochemical, mechanical, and optical properties. When secondary doped, PEDOT:PSS also achieves high values of conductivity, up to ~ 4300 S/cm due to an increase in mobile charge carriers concentration, hence it is widely used in bioelectronics as electrode interface.[34,35]

In our work, the ink is formulated starting from a water-based dispersion of PEDOT:PSS which is doped with biocompatible co-solvents, as polyethylene glycol (PEG) and EG, and enriched with carboxymethyl cellulose (CMC). PEG serves both as solid content and binder for building up 3D PEDOT:PSS/PEG microstructures and to increase conductivity, whereas EG mainly improves conductivity and acts as humectant for a controlled evaporation rate in the in-flight jet, hence avoiding dry printing.[30] Finally, CMC works as additive and binder, being an ether anionic water-soluble polysaccharide rich of hydroxyl and carboxyl groups (-COOH),[36] that promotes interaction with the functional groups of PEDOT:PSS.[37]

The final ink formulation demonstrates remarkable 2D and 3D printability capabilities at the microscale, along with high reproducibility, resolution down to ~ 35 µm, ARs ≤ 9, high conductivity (σ = 495.29 S cm^{-1} in 2D films), good electrochemical stability and superior biocompatibility. The ink especially shows a low level of cytotoxicity when in contact with different cell lineages, such as human fibroblasts (HFs) but also human-derived induced pluripotent stem cells (hiPSCs)-derived NSCs. Those values demonstrate excellent performance compared to state-of-the-art PEDOT:PSS printed microstructures. Especially, this is a novel formulation which allows the printing of a PEDOT:PSS composite in micropillars at the highest AR reported in the literature using the AJ®P technology and a PEDOT:PSS-based ink. **Table 1** offers a comprehensive comparison of PEDOT:PSS-based inks for bioelectronic applications, with a specific focus on the use of AM technologies. A review of existing literature shows a wide range of properties, with most formulations exhibiting conductivities between 3.23 [38] and 50.4 $S \cdot cm^{-1}$ [39], and few exceeding 100 $S \cdot cm^{-1}$, when reported. In contrast, our PEDOT:PSS composite ink provides a unique solution by achieving a superior conductivity of 495.3 ± 93.1 $S \cdot cm^{-1}$, which is well above the typical range. Additionally, it shows a secant compression modulus of 9.33 ± 1.8 MPa, generally higher than other reported studies but still within an acceptable range,[40] and also a sustained electrochemical stability over 20 cycles. Notably, the ink also demonstrates good biocompatibility with highly sensitive cell lines, such as hIPSCs-derived NSCs, a feature rarely reported in the literature. So far, this is highest

Table 1. Comparative Overview of PEDOT:PSS-Based Inks for 3D Microfabrication: Formulation, Electrical, and Biological Parameters.

Ink Formulation	Fabrication Method	Electrical, Electrophysiological, Mechanical Performance	Aspect Ratio	Diameter Range	Biocompatibility	Application Focus	Ref.
PEDOT:PSS + PEG + CMC + EG	Aerosol Jet® Printing	-Conductivity 495.3 ± 93.1 S·cm⁻¹ -Young's modulus ~3100 kPa per pillar -Good electrochemical activity and stability (20 CV cycles);	9	35 µm	Human fibroblasts, and hiPSC-derived NSCs	Bioelectronics, biosensing	This work
PEDOT:PSS + IL (ionic liquid)	Lithography, electron beam, water soaking for hydrogel	-Signal amplitude of 156.1 µV and SNR = 33.7 -Young's modulus ~13.4 kPa	0.59 (dry), 4.3 (hydrated)	3 µm	HL-1 cardiomyocyte cell line	Conductive hydrogel electrode for MEAs electrophysiological recording	Liu et al.[40]
PEDOT:PSS + DMSO + GOPS	Direct Ink-Writing	-Monitored cardiac tissues with ~20 µV noise and SNR 33–35 -Young's modulus 574.14 ± 108.2 kPa	50	20 µm	hiPSC cardiomyocytes	Extracellular field potential recording	Wu et al.[41]
PEDOT:PSS + EG (or DMSO) + GOPS	Direct Ink-Writing	-Conductivity 14.0–50.4 S·cm⁻¹ -Good electrochemical activity and stability (100 CV cycles), localized CV on individual pillars	Max 714 (7 µm dia., 5000 µm height)	5–20 µm	Not reported	Bioelectronics, biosensing	Zhang et al.[39]
PEDOT:PSS + Multi-walled carbon nanotubes	Aerosol Jet® Printing	Conductivity 3.23 S·cm⁻¹	3.2	10 ± 2 µm	HL-1 cardiomyocytes	Extracellular field potential recording	Zips et al.[38]
PEDOT:PSS	Electrodeposition on PDMS pillars	-Impedance ~10³–10⁴ Ω at 1 kHz - SNR=62 ± 33	1	4–7 µm	*In vivo* (adult Wistar rat)	Electrocorticography	Lunghi et al.[42]
PEDOT:PSS + sacrificial polymer	Two-Photon Polymerization (2PP) & electrodeposition	- Impedance <20 Ω (1 Hz–5 kHz)	Up to 5	1 µm	HT-22 cells	Bioelectronics, biosensing	Ruggiero et al.[43]

reported AR = 9 for PEDOT:PSS inks using the AJ®P process in a fast print time of around 10 mins for an array of 24 pillars.

This AR surpasses reported techniques for micropillars fabrication, like electrodeposition (AR = 1),[42] two-photon polymerization (AR = 5),[43] and lithography (0.6 < AR < 4.3).[40]

While direct ink writing can also produce high AR structures with AR of 50[41] or even 714,[39] the materials used often have significantly lower electrical conductivities. Overall, our work presents a major advancement by successfully integrating a high-performance material with a rapid, scalable, and maskless fabrication AM method.

Particularly, the influence of ink and machine parameters on print fidelity is verified by two full factorial design of experiments (DOEs) applied to 3D AJ®P to optimize and control the repeatability, shape fidelity and resolution of this process. Best practise print conditions are then selected to fabricate different microarray periodic structures, demonstrating the versatility of the ink formulation and printing technique selected, including dense and hollow pillars in less than 10 mins. Final micropillars also show a flexible mechanical behaviour upon microcompression, with a modulus of elasticity (E) of 9.33×10^6 Pa.

Therefore, this work introduces a novel PEDOT:PSS composite ink formulation that meets all the key requirements of a bioconductive material, here adapted to the 3D AJ®P process for the efficient production of periodic micropillar arrays. In this context, a bioconductive ink is also biocompatible and can support biological activities. This ink can have potential as electrode material or a functional interface across a wide range of applications, including biosensors and *in vitro* electrophysiology, but also lab-on-chips and *in vivo* bioelectronic devices, such as 3D MEAs, neural probes, and energy harvesting devices

2. Materials & Methods

2.1. Ink and substrate preparation

Typical AJ®P inks are nanofluids, with a loading particle size < 0.5 μm, and a wide viscosity range between [1-1000] mPa·s.[44] A water dispersion containing PEDOT:PSS at 1.3 wt% (Sigma Aldrich 483095, BE), in a weight ratio of PEDOT to PSS equal to 1:1.6, was selected as base for the ink formulation. The PEDOT:PSS dispersion was then doped with PEG (Mw = 400 Da, Sigma Aldrich P3265, BE), in variable proportions, 0.02, 0.04, 0.06, and 0.08 mol/L, in order to investigate the increase of ink conductivity. Each solution was stirred on a heating magnetic stirrer (VELP Scientifica Srl, IT) and sonicated in an ultrasonic bath (EMMI - 20 HC, Emag, DE) for 10 mins, each at RT. All formulations were then AJ®P printed and their conductivity was measured. The best solution, in terms of printability and conductivity, was further combined in a 3:2 ratio with a water-based solution of NaCMC at 0.1 w/v% (Mw = 90 kDa, Sigma Aldrich 419273, BE). The NaCMC solution was stirred in Milli-Q water for 30 mins at 60 °C and then sonicated for 10 mins at RT. To improve the printing process, EG (Sigma Aldrich 324558, BE) was then added to the solution at a concentration of 6 v/v%, functioning

as a humectant. The final ink, here referred as PEDOT:PSS composite ink, was stirred for 30 mins and further sonicated for 10 mins (both at RT), ready for printing. **Figure 1a** illustrates a schematic representation of the PEDOT:PSS composite ink. Glass slides (Superfrost, VWR, BE) were used as substrate for the printing tests. Ti/Au Si wafers were instead used for biocompatibility analyses. All the substrates were ultrasonically cleaned with distilled water (DI) and IPA (Sigma Aldrich, BE) for 15 mins at $T = 25°C$.

2.2.Fabrication process

A 3-axis U-AJ®P system AJ300s by ©Optomec (Albuquerque, USA) was used to conduct the experiments at room temperature, RT (22°C, 55%rh). Before printing, an ink volume of 850 µL was poured in a glass vial and sonicated in the ultrasonic bath at 25°C for 10 mins at a power atomization of 48 V. If necessary, ink refilling was conducted every 3 h of continuous printing to allow a stable aerosol deposition.

Figure 1b reports the ultrasonic U-AJ®P process flow. The U-AJ®P process is limited to low viscous inks, with a viscosity in the range of [1-10] mPa·s, [24] and it is usually divided

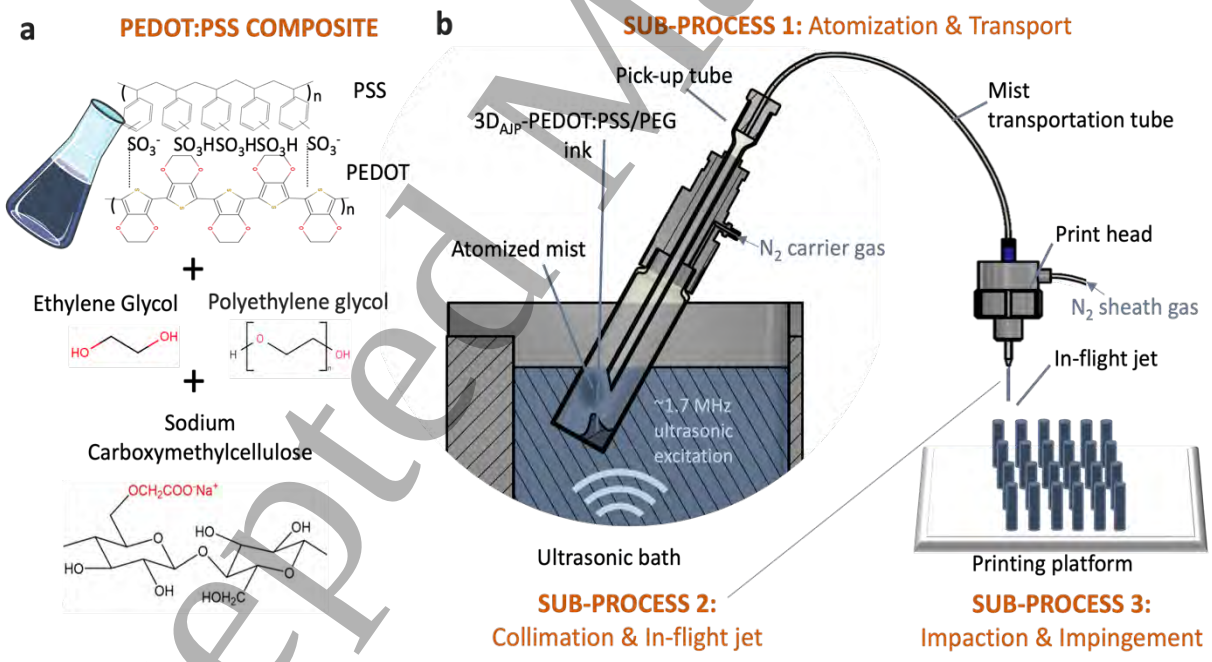

Figure 1. Schematic representation of the a) PEDOT:PSS composite ink composition and b) 3D-AJ®P process, highlighting the three main phases: i) atomization and transport of the aerosol mist, ii) collimation and in-flight jet, and iii) impaction and impingement of the aerosol jet through a nozzle onto the substrate. Figure adapted from Degryse et al., International Conference on Biofabrication, 2022.[45] Parts of the figure were generated by using Servier Medical Art. by Servier, Creative Commons Attribution 3.0 Unported License.

in three main phases: aerosol mist generation from a liquid dispersion, transport and collimation of the mist into a focused aerosol jet, and, finally, its deposition on the desired substrate.

In the ink reservoir, a transducer submerged in a transfer medium (here distilled water) generates high frequency ultrasonic waves, up to 2.4 MHz.[46] Oscillations and perturbations are formed on the surface of the ink poured in a glass vial, until the liquid surface disintegrates into ligaments and further into a mist composed of micro-droplets. This mist is then accelerated and transported to the print head in a plastic tube by means of an inert gas (nitrogen, N_2), referred as carrier gas flow, *CGF* = (0 – 50) [sccm]. In the print head, the mist is then aerodynamically collimated into an aerosol beam by means of an annular inert gas (N_2), called sheath gas flow, *SGF* = (0 – 200) [sccm]. Subsequently, the aerosol jet is directed on the substrate through a nozzle of a specific diameter *Ø* [µm], at a selected stand-off distance, *z* = (1 -5) [mm]. The in-flight jet from the exit of the nozzle impinges and coalescences on the target substrate. Printed test trials were performed to reduce any system drifting within the first 5 to 10 mins. In addition, the substrates were kept on the platform for at least 10 mins before printing, to ensure a thermal equilibrium between with the platen temperature, which can be heated up till 200 °C. After printing, all samples were thermally annealed at *T* = 140°C for 1h (Heraeus over, DE) to allow complete evaporation of the co-solvents.

2D printing tests. PEDOT:PSS-based inks doped with PEG, in variable proportion (0.02, 0.04, 0.06, and 0.08 mol/L), as conductivity enhancer was AJ® printed in 2D squared electrodes (8 x 8 mm, trace line 0.08 mm) on glass slides (Superfrost VWR, BE). A total of eight ink formulations were tested. The main print parameters used were: nozzle diameter, *Ø* [µm] = 300 µm, *Rf* [#] = 2 (with *SGF* [sccm] = 80 sccm and *CGF* [sccm] = 40 sccm), print speed, *s* [mm/s] = 25 mm/s, *T* [°C] = 40 °C, and *n* [#] = 10. The samples for the biocompatibility tests were printed using the same printing settings on Au/Ti substrates. At least three repetitions for each experiment were conducted. The electrical conductivity and biocompatibility characterisation is reported in *Section 3.2.*

3D printing tests. Each sample was printed according to a layer-by-layer (LBL) strategy, starting for a CAD pattern, composed of an array of 6 x 4 circles, each circle with a diameter

Table 2. Experimental tests on the 3D-LBL AJ® printing of micropillars using the PEDOT:PSS composite ink. Two full factorial design of experiments are performed for screening and optimisation of the process window, by varying C*GF* and *Rf*, with response of interest the Printability and Shape Fidelity Index, Ψ [#] (**Figure SI.3**). Three repetitions per condition are conducted.

1st Design of Experiment for PEDOT:PSS composite printed micropillars -screening						
Factors	**Levels**					
Carrier gas flow, *CGF* [sccm]	20	25	30	35	40	45
Focusing Ratio, *Rf* [#]	1-2-3-4	1-2-3-4	1-2-3-4	1-2-3-4	1-2-3-4	1-2-3-4
Repetitions [#]	3					
2nd Design of Experiment for PEDOT:PSS composite printed micropillars						
Factors	**Levels**					
Carrier gas flow, *CGF* [sccm]	20		22.5		25	
Focusing Ratio, *Rf* [#]	1.2-1.4-1.6		1.2-1.4-1.6		1.2-1.4-1.6	
Repetitions [#]	3					
General Response	Printability and Shape Fidelity Index, Ψ [#]					
Fixed Parameters	**Values**					
Sample design	Array of 6x4 circles, $\emptyset$ = 50 µm					
Substrate	Glass slides, VWR Superfrost® Plus Micro Slide					
Nozzle diameter, $\emptyset$ [µm]	150					
Stand-off distance, *z* [mm]	3					
Platen temperature, *T* [°C]	80					
Number of layers, *n* [#]	25					

of 50 µm and at an inter-space distance of 90 µm. From the CAD file, a .prg toolpath code was obtained by means of VM Tools (©VMware inc., USA). First, a multi-level DOE at 2 factors was executed as screening method to study key selected parameters (three repetitions per data point). The two factors analysed were *CGF* at 6 levels (20; 25; 30; 35; 40; 45) sccm and *Rf* at 4 levels (1; 2; 3; 4) (exploded into 6 sub-combinations of *SGF* and related *CGF*) for a total of 24 points (72 arrays, 1728 pillars, 3 pillars/sec), as a means to cover the complete parameter window of the machine in terms of *CGF* (0 - 50) sccm. The levels are here intended as the number of discrete values assigned to each factor analysed.

Based on the results obtained, a second DOE was performed on a narrower working window, limited by *CGF* (20; 22.5; 25) sccm and *Rf* (1.2; 1.4; 1.6), respectively, for a total of 9 points (27 arrays, 648 pillars). The details of each experiment are reported in **Table 2**. A nozzle diameter, $\emptyset$ = 150 [µm], and a number of printed layers, *n* [#] = 25, were chosen for the investigation. The platen temperature was set at *T* [°C] = 80 °C to enhance in-situ evaporation of the ink (co)-solvents and allow building up the 3D micropillars.

2.3. Ink characterization

The density, ρ, and viscosity, μ, of the PEDOT:PSS composite ink were assessed by means of a density meter and a rolling ball viscometer (DMA 4100M and Lovis 2000M, Anton Paar, AT), respectively. At least 1 mL of ink was poured into the density meter for the density measurement,

while for viscosity, the ink was loaded into a 1.8 mm capillary tube containing a gold ball, using a syringe and the proper adapter. All data were recorded at 20, 30, 40, 50, and 60°C, at an inclination angle of 70°, and with at least 3 repetitions. The same equipment was then used to measure the surface tension, γ, of the ink using a droplet volume of 14 uL, at RT. Zeta potential (ZP) and dynamic light scattering (DLS) measurements of the PEDOT:PSS composite ink were performed, using a particle size analyzer (Litesizer 500, Antoon Paar, Gmbh) at pH = 7, and assuming a spherical shape of the particles. The ink was tested under fresh conditions and after one month of shelf time, to assess particles agglomeration. Fourier transform infrared (FT-IR) spectroscopy was executed on the ink in powder form by means of a Compact FT-IR spectrometer (Alpha II Bruker, USA), with the spectra in the range of [400–4000] cm^{-1}. On a petri dish, 3 mL of each sample were drop-cast and thermally annealed for one hour at 140 °C. Afterwards, the material was cooled down and shredded into powder. Thermogravimetric analyses (TGA) of the ink before and after printing were performed on a SDT Q600 system (TA instruments, BE) under air atmosphere (100 mL/min) and at a linear heating rate of 10 °C/min up to 300 °C. Contact angle (CA, [°]) (Contact Angle Goniometer, Ossila, UK) measurements of the PEDOT:PSS composite ink were carried out on glass slides at two time points, t_1 = 5 s and t_2 = 30 s, using a 25µl glass syringe.

2.4. Printed films characterization

The sheet resistance, R_{sh} [Ω/sq], of the printed squared electrodes was recorded three times per sample by means of a four-point probe system (Ossila B.V., NL). Profilometer analyses of the printed constructs were performed using a Dektak XT Stylus Profiler (Bruker, USA) to obtain the thickness t [µm] of each 2D printed film (three repetitions each). The conductivity, σ [S/cm], of each ink was calculated using the following equation:

$$\sigma = \frac{1}{t \, x \, R_{sh}} \qquad (1)$$

Raman spectroscopy was performed on 2D-AJ® printed PEDOT:PSS composite samples, while cyclic voltammetry (CV) analyses were performed on drop-casted PEDOT:PSS composite samples using a Gamry Reference 600™ (USA). The measurements were carried out using a three-electrode setup, with a Pt wire as counter electrode (CE) and Ag/AgCl as reference electrode (RE). The ink was drop casted on a Pt disc (Ø = 3 mm) working electrode (WE) and annealed at 140 °C for 1 h in a thermal oven (Heraeus, DE). After cooling, the samples were tested in a 1x PBS electrolyte solution at an applied voltage between -0.5 and +0.8 V, at multiple

scan rates k [mVs^{-1}] of 20, 50, 100, 150, and 250 mVs^{-1}, at a step size of 1 mV, and for 20 cycles. The specific capacitance C_{sp} [F/g] was calculated using the formula reported as follows:

$$Csp = \frac{\int idV}{2 \cdot m \cdot k \cdot \Delta V} \qquad (2)$$

In Equation 2, the integral $\int idV$ represents the area of the CV curves, m [g] is the mass of the material under analysis, k is the scan rate, and ΔV [V] is the potential window. At least 3 repetitions per test were performed.

2.5. Printed micropillars characterization

The PEDOT:PSS/PEG formulation with the highest σ was further optimized for the printing of 3D micro-structures. To achieve a quantitative analysis from the observations on the pillar's quality, a Printability and Shape Fidelity Index, Ψ [#], $0 \leq \Psi \leq 1$ was calculated as the arithmetic mean of four sub-indices, to validate visual observations.[47] The four sub-indices examined are: i) the uniformity index, i_u [#], ii) the aspect ratio index, i_{AR} [#], and iii) the bending angle index, i_α [#], and the iv) Line Edge Roughness (LER) index, i_{LER} [#]. Each sub-index is calculated between 0 (best condition) and 1 (worst condition), being 1 resembling the geometry of an exact cylinder. Particularly, the first index, i_u, calculates the average of normalized ratios for each diameter difference relative to the top, middle, and base diameters; the aspect ratio index, i_{AR}, computes the absolute ratio of the greater value between the top and base diameter (ϕ) to the height (h); the bending angle index, i_α, calculates the absolute value of the normalized difference between an angle of $\pi/2$ and the measured angle α; ultimately, the index, i_{LER},[48] is a mathematical parameter used to characterize the edge surface quality, and it was calculated as the standard deviation of the pillar edge position (l^{th}) relatively to the mean pillar edge. **Figure SI.1** (Supporting Information) illustrates the sub-indexes calculations as a function of the geometrical metrics. The metrological analysis was conducted through visual inspection using an optical microscope (Hirox KH 8700, JP) and a scanning electron microscope (SEM) (VEGA3 Tescan, PRAG). For each point, the front raw of the 3D-LBL AJ® printed array composed of 6 pillars was inspected. The geometrical dimensions were assessed with the image analysis software ImageJ. Micro-compression tests were performed on the best 3D printed pillars, using a LM-1 (Bose, USA) test bench equipped with a Dino-Lite Digital Microscope (Taiwan). Micropillar arrays were positioned on the plate and aligned using the Dino-Lite camera at the centre of the actuator, with a preload cell of 0.01 N and using a displacement control test at 100 Hz. A load cell with a maximum capacity of 1.8 N at a compression rate of 5 µm/s were selected and at least three samples for each condition were measured. PEDOT:PSS

composite pillars (Φ = 50 μm at n = 30) were printed as an array of 4 x 4, disposed at 200 μm. For the stress calculation, the total area was obtained by multiplying the cross-sectional area of a single pillar by 16. Stress-strain curves were then derived from the data acquired.

2.6. Biocompatibility assays

Cellular viability and proliferation of 2D-AJ® PEDOT:PSS composite printed films was assessed by direct and indirect viability assays, using HFs and hiPSCs derived in neural stem cells (NSCs). A commercial HFs line (BJ cell line ATCC® CRL-2522™) was cultured with the addition of complete DMEM (DMEM supplemented with 10% fetal calf serum and 100 units/mL penicillin/streptomycin, Euroclone), and incubated for 30 min. A commercial human iPSCs control cell line (Gibco™ episomal hiPSC line, cat. n. A18945, ThermoFisher Scientifc, Inc., Waltham, MA, USA), was also induced and characterized in NSCs, according to the protocol described by Ferraro et al.[49] All samples were washed with PBS and then sterilized using an autoclave at 121°C before cell culturing. Three repetitions were tested per cellular line, condition and time point. The PEDOT:PSS composite ink was AJ® printed as the samples prepared for conductivity tests. The biocompatibility of the ink was detected, using both direct and indirect ATP assays (CellTiter-Glo® 3D Cell Viability, G968, Promega Srl, IT) on NSCs at 24, 48, and 96 h, according to the supplier instructions. Per time point, three repetitions were carried out and plastic was used as positive control. For the direct ATP viability assay, a concentrated NSCs suspension of 6×10^4 cells cm^{-2} was placed on the printed ink and incubated at 37°C, 5% CO_2 for 30 minutes and then filled up with Neural Expansion Medium (PSC Neural Induction Medium diluted 1:1 with Advanced DMEM/F-12 Thermo-Fisher Scientific). Later, cell lysis was induced on each sample by filling it with the CellTiter-Glo 3D Reagent at a volume equal to the cell culture medium one. The samples were then left for 25 mins at RT to stabilize the luminescent signal. The solution was transferred in a 96-well opaque plate, and luminescence recording was performed by means of a Microplate Reader Infinite 200 (Tecan Group Ltd., CH). Finally, an ATP standard curve was plotted in the range of 10 μM to 10 nM, using the ribonucleoside triphosphate (r)ATP (P1132, Promega Srl, IT) to compare the luminescence values acquired from the standard wells and the samples. Hence, the ATP concentration was calculated and plotted. For the indirect ATP viability assay, the printed samples were instead placed in a 24-well plate, covered by 1 mL of Neural Expansion Medium, and kept for 5 days in the incubator, to release any potential cytotoxic compound. As internal control, the same amount of medium culture was stored at the same conditions in an empty 24-

well plate. Parallelly, NSCs were seeded in coated flat bottom 48-well plates at a concentration of 6×10^4 cell cm^{-2} in Neural Expansion Medium. The day after, cells supernatant was discarded and changed by either the conditioned medium collected by the printed samples or the control medium. NSCs were also cultured with fresh medium and on a Matrigel coating as a positive control to confirm that the neural medium stored in the incubator for 5 days did not affect cell health. The same procedure applied for the direct test was then pursued.

Immunofluorescence tests were carried out to detect the cellular morphology (nuclei and cytoskeleton) and adhesion of HFs and NSCs seeded on the printed ink. A coating of Matrigel (Corning, USA) was drop casted on the printed samples and kept for 1 hour at 37°C. The NSCs suspension was seeded on the samples and plastic control, at a concentration of: HFs, 5×10^5 cells cm^{-2}; NSCs, 6×10^4 cells cm^{-2}, and then placed in the incubator. After 30 mins, each construct was filled with a relative volume of DMEM or Neural Expansion Medium and stored back in the incubator. At 48 hours of cell culturing, cells were fixed and permeabilized with the Fix&Perm Sample Kit® (SIC) for 30 mins. Afterwards, a blocking solution (iBindTM ×5 Buffer, Invitrogen, USA) was poured on the samples in the incubator for 45 mins. Later, the samples were stained with Phalloidin (Sigma Aldrich, IT) and counterstained for 5 mins with Hoechst 33342 to detect cellular cytoskeleton and nucleus, respectively. Finally, a drop of glycerol was poured on the top of the specimens disposed on glass coverslips. The immunofluorescence was studied using an inverted fluorescence microscope (IX70, Olympus, USA) and the Image-Pro Plus software v.7.0 (Media Cybernetics Inc., USA).

2.7. Statistical analysis

Statistical analyses were performed using Minitab® 2024 (Minitab LLC, State College, PA, USA). The analysis included analysis of variance (ANOVA) and main effects plots. Comparisons between groups were performed by Student's t-test, using GraphPad Prism (San Diego, CA). Data from replicates were expressed as mean ± standard deviation.

3. Results

3.1 PEDOT:PSS composite ink

The PEDOT:PSS composite ink was selected from a total of eight formulations starting from a PEDOT:PSS water dispersion, doped with PEG at 0.02, 0.04, 0.06, and 0.08 mol/L concentrations, successfully atomized and printed as squares (8 x 8 mm, trace line 0.08 mm) on

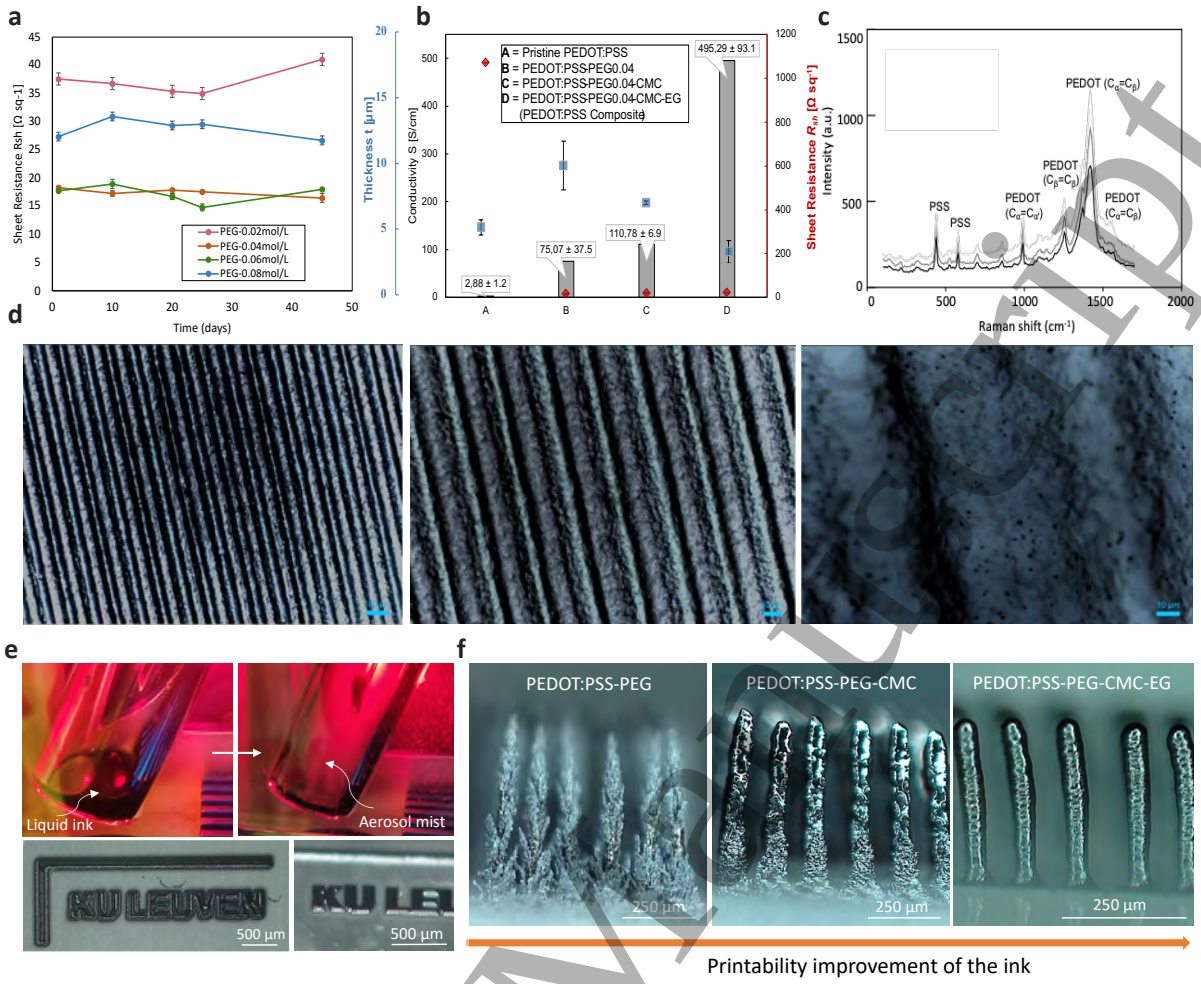

Figure 2. Representative. images of (a) sheet resistance R_{sh} from day 0 to day 45 of 2D-AJ® printed thin squares, for each PEG concentration (0.02, 0.04, 0.06, and 0.08 mol/L), (b) conductivity enhancement σ, along with R_{sh} and t measurements, of 2D-AJ® printed inks from pristine state to the final composition PEDOT:PSS composite; (c) Raman spectra of 2D-AJ® printed PEDOT:PSS composite films; (d) microscopy images of 2D-AJ®printed PEDOT:PSS composite samples at scales; (e) PEDOT:PSS composite ink in its liquid-aerosol mist states before and after aerosolization at 15 mins of continuous sonication (49.5 V) and a 2D printed KU Leuven Logo; (f) 3D-AJ®P of micropillars at different formulations at a platen temperature of 80°C: PEDOT:PSS-PEG, PEDOT:PSS-PEG-CMC, and PEDOT:PSS-PEG-CMC-EG (PEDOT:PSS composite ink).

glass slides. The sheet resistance, R_{sh}, of each sample was recorded from day 0 till day 45 (**Figure 2a**). The PEDOT:PSS-based ink was systematically formulated by optimizing each solvent and additive in order to achieve a right balance among high conductivity, mechanical stability, and 3D printability. PEG was added as the primary solid content and conductivy dopant. Particularly, PEG is used as main solid component, providing both conductivity and structural integrity for the micropillars, while EG is primarily used as humectant during printing to avoid drying the pillar surface and as conductivity dopant. To generate such micropillars, four concentrations of PEG (0.02, 0.04, 0.06, and 0.08 mol/L) were tested, showing that the highest conductivities were achieved with 0.04 mol/L (σ = 75.07 S·cm^{-1}) and 0.06 mol/L (σ =

74.66 S·cm⁻¹) (**Figure 2a**). The 0.04 mol/L PEG concentration was ultimately chosen for the final formulation because it demonstrated comparable electrical performance and slightly lower sheet resistance (*Rsh* = 18.28 ± 0.5 Ω/sq), providing a reproducible and stable baseline. To further improve the mechanical integrity and printability of the 3D structures, a concentration of 0.1 w/v% of CMC was added in the ink. This concentration was chosen based on prior literature, which typically refers to 0.1 w/v%,[50] and it was found acceptable to provide the ink with the necessary viscosity to maintain the 3D micropillar shape after printing and sufficient electrochemical stability.[51] A 0.1 w/v% of CMC also generated a stable and homogeneous dispersion with the PEDOT:PSS/PEG dispersion. EG was finally included at 6 v/v% to mainly control the evaporation rate during the in-flight AJ®P process, preventing premature drying and uniform deposition, and to boost the final ink conductivity. It is important to note that EG alone, without PEG, would not support the formation of stable micropillars, as it is almost removed after annealing, but it drastically improves the micropillars surface roughness, as further shown in **Figure 2f**. The EG concentration was set at 6 v/v%, in line with values reported in the literature and commonly used in commercial ink formulations (typically 2–10 v/v%), to enhance conductivity.

The density of the final PEDOT:PSS composite was equal to ρ = 0.99 ± 0.01 g/cm³, being the main solvent MilliQ water, while the dynamic viscosity was detected around μ = 7.93 mPa·s at T = 20 °C, in accordance with the theoretical upper bound for a U-AJ®P process. By increasing T from 20 °C to 60 °C, the viscosity lowered, reaching a minimum value of μ = 3.45 mPa·s. Furthermore, the final fresh PEDOT:PSS composite ink presented an average hydrodynamic diameter of 15.95 ± 4.7 µm with a polydispersity index (PDI) of 36.13%, while in its 1-month version a diameter of 33.28 ± 10.6 µm with a PDI 43.87%, respectively.

The ink surface tension was equal to γ = 71.55 ± 0.17 mN/m (pristine PEDOT:PSS γ = 53.7 ± 2.8 mN/m), which is similar to demi water at RT. **Figure 2b** depicts the increase of ink conductivity starting from its initial pristine state (A) and progressing (B-C) to the final ink formulation (D). The conductivity of the ink is equal to σ = 495.29 S cm^{-1} (with R_{sh}, of 24.34 Ω/sq ± 0.1 Ω/sq and t = 0.83 µm ± 0.1 µm), showing a substantial increase compared to pristine PEDOT:PSS ink (σ = 2.88 S cm^{-1}). Raman spectra of 2D-AJ® printed PEDOT:PSS-based films under laser excitation (633 nm), verify the presence of PEDOT and PSS spectra: vibrational modes of PSS are found at 1110 cm^{-1} and 1000 cm^{-1}, while PEDOT vibrational modes, which correspond to the Cα = Cβ asymmetrical, Cα = Cβ symmetrical, Cβ = Cβ stretching, and Cα = Cα' inter-ring stretching, are situated at 1524 cm^{-1}, 1452 cm^{-1}, 1383 cm^{-1}, and 1272 cm^{-1}.[52]

Raman fingerprints of PEG are also visible, especially at 527 cm^{-1}, 864 cm^{-1} (C-O-C bond), 1130 cm^{-1} (C-C bond), and 1238 cm^{-1} (CH2 bond) (**Figure 2c**).[53]

The PEDOT:PSS/PEG ink was then successfully AJ® printed in 2D, with visible print patterns at different scales (**Figure 2d**). The aerosol formed after 15 mins of continuous sonication at 49.5 V is visible in **Figure 2e**. The printing of complex 2D profiles, such as the KU Leuven logo, is also demonstrated. The 3D AJ® printability of the ink, along with intermediate formulations: PEDOT:PSS-PEG; PEDOT:PSS-PEG-CMC and PEDOT:PSS-PEG-CMC-EG (*namely,* the PEDOT:PSS composite) is instead shown in **Figure 2f**.

FTIR analysis on printed PEDOT:PSS composite after annealing, detects typical stretching vibrations of the -OH and C- groups, observable between 3200 and 3500 cm^{-1}, and at the peak at 2860 cm^{-1}, respectively (**Figure 3a**). The spectra also indicate main shifts compared to pristine PEDOT:PSS, considering: i) reduction of PEDOT:PSS content, ii) presence of EG (molecular structure $HO–CH_2–CH_2–OH$) and PEG functional groups, visible

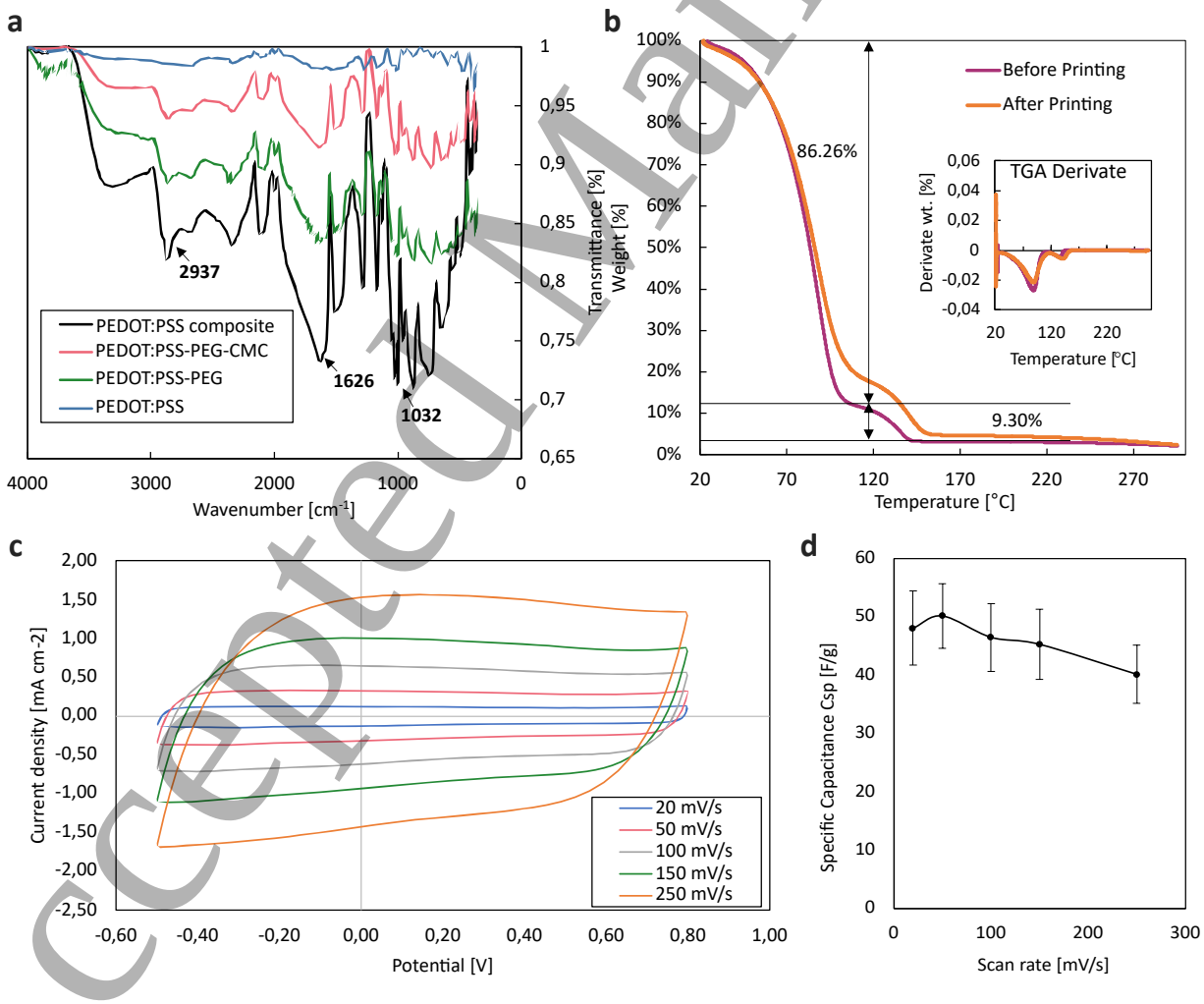

Figure 3. Representative graphs of (a) FTIR spectra, (b) TGA thermogram, and (c) cyclic voltammetry analysis, along with (d) specific capacitance of the PEDOT:PSS composite ink.

by a decrease of the band intensity at 1023 cm^{-1}, due to the stretching of OH and COH, and by the peak at 2937 cm^{-1}, corresponding to C-H stretching vibrations [54]; iii) an absorption band at 1626 cm^{-1}, correlated to the stretching vibration of the carboxylic acid group in CMC.[55]

Both TGA before and after printing, indicate a two-stage weight loss (**Figure 3b**): i) a first weight loss (~88%) up to 100 °C, attributed to water evaporation; and ii) a second weight loss between 100 °C and 150 °C (> 96%), related to the (co)-solvent mass loss (normal boiling point, NBP of EG = 198 °C). This loss was caused by the escape of volatile components, such as water and carbon dioxide. PEG remains in the ink after processing, as its NBP is 250 °C. Afterwards, PEDOT:PSS, PEG and CMC (NBP = 525 °C) start degrading. The TGA derivative graph also shows comparable curves.

CV curves on PEDOT:PSS composite films exhibit a pseudo rectangular mirror image indicating a good capacitive behaviour and a constant diffusion rate.[56] (**Figure 3c**). At higher scan rates (150, and 250 mV/s), the curves undergo a broad expansion, still recalling a double-layer capacitor behaviour.[57] The trend of the PEDOT:PSS composite specific capacitance (C_{sp}) is presented in **Figure 3d,** as a function of the applied scan rates, at a m = 0.1 mg.

3.2 Process and printability analysis

The PEDOT:PSS composite ink was further tested for printability in 3D microstructures. Firstly, the ink demonstrated a good adhesion with the reference glass substrate, with a measured CA equal to CA_{t1} = 54.10 ± 2.5° and CA_{t2} = 46.27 ± 4.5°, ideal for the AJ®P technology (CA of pristine PEDOT:PSS = 43.4° ± 2.9°).[8]

Secondly, DOE approaches were applied to investigate the printability of the ink in 3D. From **Figure 4**, it is evident that not all parameter combinations resulted in a successful fabrication of micropillars. Particularly, **Figure 4a** illustrates the printing of micropillars at different combinations of *CGF* = [20,25,30,35,40,45] sccm and *Rf* = [1,2,3,4]. Specifically, the *CGF* indicates the amount of aerosol mist transported to the deposition head, while *Rf* defines the intensity of jet focusing at the nozzle exit. The focusing ratio, *Rf*, is a crucial parameter in AJ®P and it is defined as the ratio between the sheath gas flow *SGF*, which aerodynamically focuses the jet in the deposition head, and the *CGF*, which affects the mass flow rate of the jet ($Rf = \frac{SGF}{CGF} \geq 1$ for a converged jet). The favourable conditions that resulted in the successful printing of micropillars have been alphabetically labelled from A to L, while NA refers to *not*

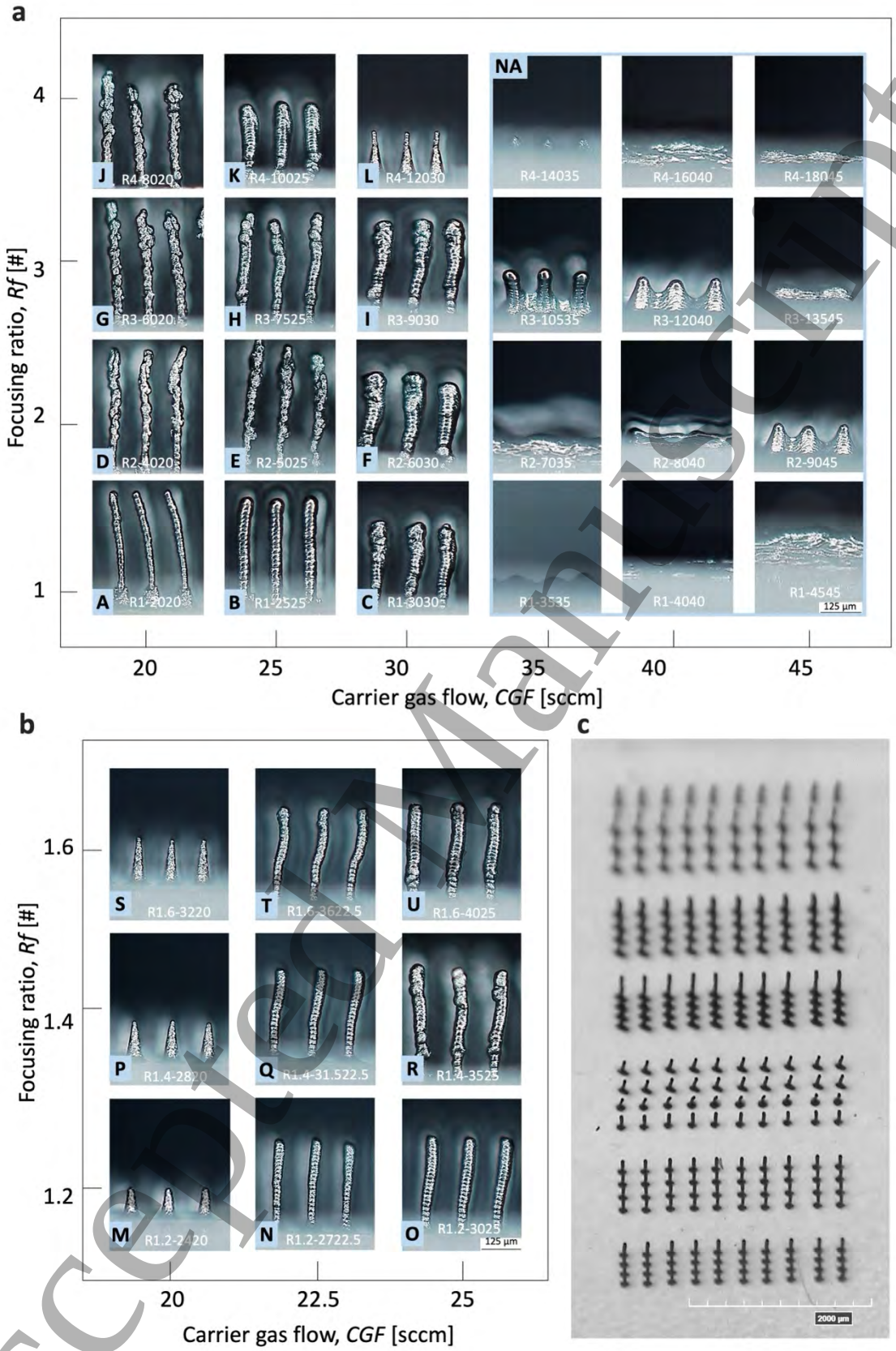

Figure 4. Representative results and experimental conditions of the full factorial designs applied to the PEDOT:PSS composite ink in fabricating micropillars: a) screening design; b) optimising design. (N = 3, subsample equal to 24 pillars); (c) feasibility study in fabricating periodic arrays of micropillars via 3D AJ®P and the own developed PEDOT:PSS composite functional inks; the compositions comprehends > 300 pillars of different heights.

applicable conditions. A print time of around 7 mins was necessary per micropillar array (24 pillars with $n = 25$ layers, approximately 0.7 s/layer).

When a *CGF* is ≥ 35 sccm, the typical results are merged micropillars or material deposition in undefined shapes. On the other side, a *CGF* < 35 sccm leads to the formation of distinctive micropillar structures, regardless *Rf*. Moreover, not all structures meet the desired criteria of a cylindrical shape, with straight and smooth surfaces. Such micropillars can be only achieved at low *CGF* and *Rf* settings, especially at the conditions A (R1-2020) and B (R1-2525, preferred one), in which nearly every printed layer is visible. The combination *CGF* = 30 sccm and low *Rf* instead produce larger micropillars. In certain cases, especially at low *CGF* and high *Rf* (which is equal to high sheath gas flow *SGF*), the micropillars also exhibit irregular surfaces characterized by multiple bumps (see D (R2-4020), G (R3-6020), E (R2-5025), and H (R3-7525).

A narrower process window was then investigated to optimize the printing process, with *CGF* within [20, 22.5, 25] sccm and *Rf* [1.2, 1.4, 1.6] (**Figure 4b**). The conditions were alphabetically labelled from M to U. This parameter window is centred around the previously identified printing parameters that resulted in the most favourable outcomes, with $1 \leq Rf \leq 2$ and $20 \leq CGF \leq 25$ sccm. Among the nine conditions tested, the most promising results are obtained when *Rf* is set to 1.2 and *CGF* is either fixed at 22.5 sccm, N (R1.2-2722.5) or 25 sccm, O (R1.2-3025). The observations underline the necessity to set *CGF* ~ 25 sccm and *Rf* ~ 1 to achieve cylindrical, straight 3D printed micropillars.

Micropillars shape fidelity was evaluated considering pillars height, h [μm], bending angle, α [rad], the mean diameter Φ [μm] (mean between top, middle and bottom Φ), and the *LER* [μm]. Among the parameter combinations that successfully resulted in micropillar formation, the highest achieved pillar height, h [μm], was recorded at $h = (433.25 \pm 13.5)$ μm, with a middle $\Phi = 42.85 \pm 4.1$ μm and an $AR = 8.5$, under the condition D. Values are reported in **Table SI.1**, Supporting Information. Conversely, the lowest pillar height observed was $h = 101.45 \pm 3.2$ μm, which occurred at condition M (R1.2-2420), with a middle $\Phi = 34.61 \pm 1.1$ μm and an $AR = 1.88$. The bending angle α, was more than consistent across the conditions, falling within a narrow range of $1.25 \leq \alpha \leq 1.69$ rads for all tested cases. On the other hand, the diameter of the micropillars displayed more noticeable variations thorough the length, particularly evident in the conditions F (R2-6030, top $\Phi = 20.03 \pm 1.4$ μm, middle $\Phi = 37.16 \pm 2.6$ μm, and base $\Phi = 59.13 \pm 3.9$ μm), P (R1.4-2820, top $\Phi = 18.28 \pm 0.7$ μm, middle $\Phi = 35.27 \pm 1.9$ μm, and base $\Phi = 57.74 \pm 3.3$ μm), and S (R1.6-3220, top $\Phi = 19.41 \pm 2.0$ μm,

middle Φ = 35.94 ± 2.1 μm, and base Φ = 57.12 ± 2.4 μm), where the Coefficient of Variation (Cv) exceeds 41%. Conversely, in the other two cases (P and S), the variations in pillar diameter are related to the conical shapes (**Figure 4**). A Cv of 10% is instead achieved in the conditions B, N, and Q. These conditions were also previously identified as the most favourable, based on the combination of geometry and shape. Among them, the condition B shows the minimum variation from the CAD file, which is a circle with $\emptyset$ = 50 μm, having a $\emptyset_{avg}$ = (55.52 ± 5.6) μm. Regarding LER, when the pillars exhibit wavy edges, LER tends to result in higher values, and vice versa. For instance, conditions G and R (R1.43525) exhibit the highest LER values, with LER_G = (14.72 ± 1.2) μm and LER_S = (14.53 ± 1.9) μm. As depicted in **Figure 4**, these pillars display irregularities and bumps on their edge surfaces. Contrarily, conditions M, N, and S (with *CGF* = 20 sccm) demonstrate the lowest LER values within the range of $3.99 \leq LER_{N,Q,T} \leq 5.2$ μm, primarily due to their conical shapes. At *CGF* = 20 sccm, the structures exhibit a conical shape, most likely because the reduced material flux onto the substrate prevents the formation of fully developed micropillars. This morphology was consistently observed across multiple replicates (three sets of six pillars each), highlighting the inherent variability of the process under these conditions and the necessity to use higher *CGF* values. Instead, conditions F, N, and O, show promising LER values and in fact show smooth surfaces.

The Printability and Shape Fidelity Index, Ψ [#], $0 \leq \Psi \leq 1$ was calculated as mean of the sub-indexes i_u, i_{AR}, i_α, i_{LER}. The i_u index evaluates the consistency of diameter length along the micropillar height, the i_{AR} index favours high AR (ideal = 0), the i_α index considers the deviation from an angle of π/2, and, finally, LER characterizes the edge surface quality. **Figures SI.3a and SI.3b** (Supporting Information) report the values of the arithmetic Ψ_A and sub-indices for screening ($\Psi_{A,S}$) and focused ($\Psi_{A,F}$) windows, respectively. The least impact on Ψ is denoted by the bending angle i_α, with values in the range of $0.002 \leq i_\alpha \leq 0.018$, while the second least factor is the aspect ratio index i_{AR}, with values among $0.101 \leq i_{AR} \leq 0.531$. Likewise, the uniformity index i_u demonstrates higher significance for conditions M, P, and S, with P being the worst one ($0.159 \leq i_u \leq 0.708$). Conditions U, N, and Q have the most favourable values in this regard. The most significant factor is the line edge roughness index, i_{LER}, with peaks in G and R at i_{LER} = 0.899 ± 0.075 and reaching a minimum in M and P, where i_{LER} = 0.241 ± 0.02. The lowest value of Printability and Shape Fidelity Index is equal to Ψ = 0.169, achieved under the condition N, characterized by a *Rf* = 1.2 and a *CGF* = 22.5 sccm. Conversely, the highest value, Ψ = 0.380, is attained under the condition F, featuring a *Rf* = 2, and a *CGF* = 30 sccm. **Figure 4c** demonstrates the feasibility of 3D AJ®P periodic arrays at the optimal condition,

consisting of over 300 pillars with different heights. The variations in pillar appearance are partly due to their intentionally different heights, which result from printing different numbers of layers.

Figures 5a and 5b present contour plots with linear interopolation illustrating the relationship of $\Psi_{A,S}$ and $\Psi_{A,F}$ windows, with respect to *CGF* and *Rf*. Both contour plots confirm the presence of minimum values for $\Psi_{A,S}$ when $Rf \leq 1.5$ with $CGF \leq 25$ sccm, and for $\Psi_{A,F}$ in the specific region where $Rf \leq 1.5$ and $22 \leq CGF \leq 24$ sccm. The contour plot of $\Psi_{A,S}$ also highlights that a $CGF \geq 28$ sccm tends to increase the value of $\Psi_{A,S}$. The probability plots (normal distributions) for $\Psi_{A,S}$ and $\Psi_{A,F}$, are reported in **Figures 5c** and **5d**, respectively. The main effect plots for $\Psi_{A,S}$ and $\Psi_{A,F}$ are also presented in **Figures 5e** and **5f**. Particularly, when *Rf* is set to 1, lower values of $\Psi_{A,S}$ are achieved, supported by a P-value $P_{Rf} = 0.002$ (ANOVA).

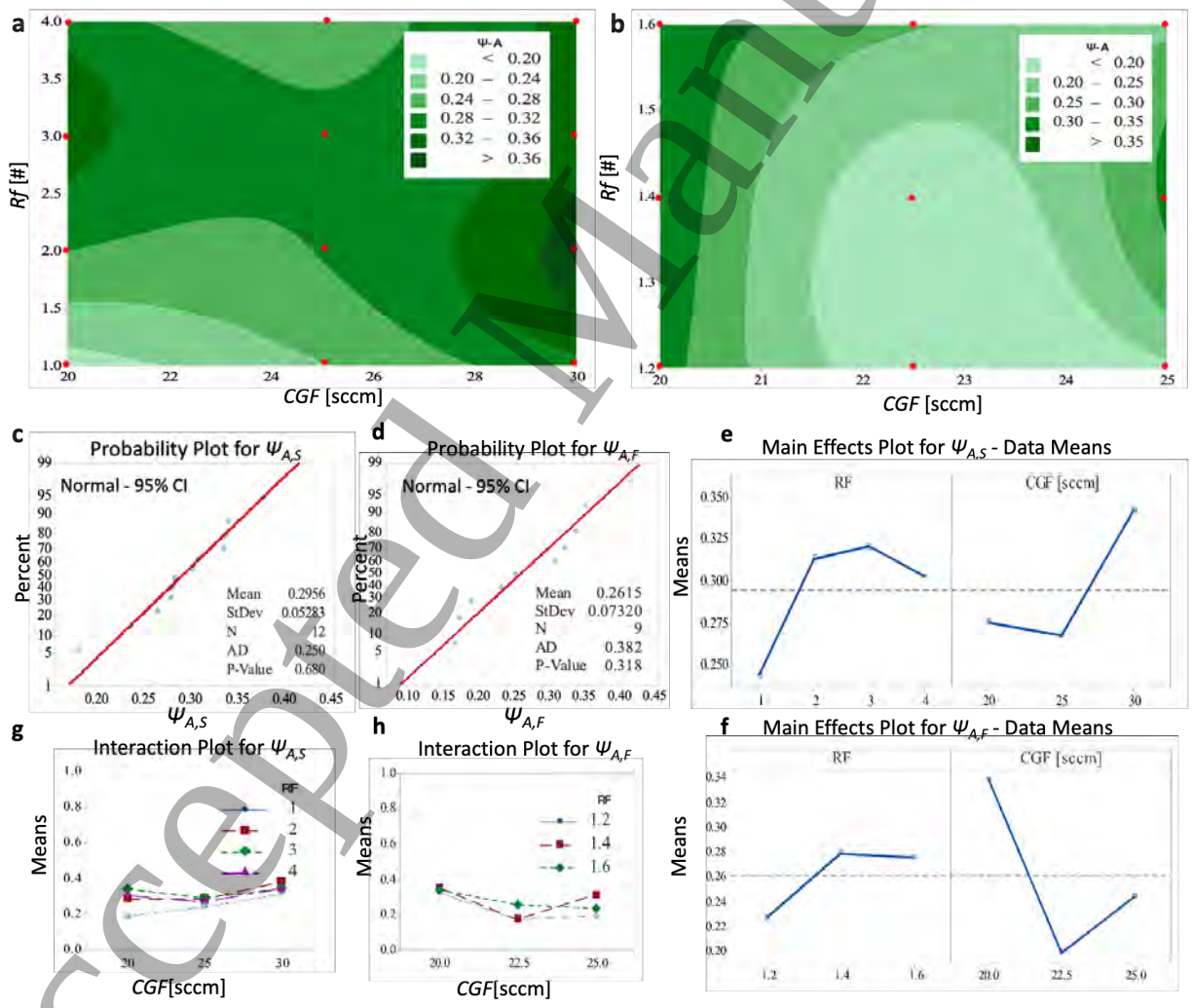

Figure 5. Results obtained from the statistical analysis of Ψ, indicating the contour plots for (a) $\Psi_{A,S}$ and (b) $\Psi_{A,F}$ (red marks representing experimental data points), the normality plots for (c) $\Psi_{A,S}$ and (d) $\Psi_{A,F}$, the main effects plots for (e) $\Psi_{A,S}$ and (f) $\Psi_{A,F}$, and the interaction plots for (g) $\Psi_{A,S}$ and (h) $\Psi_{A,F}$.

The *CGF* has instead a lower statistical significance than *Rf*, with a $P_{CGF} = 0.04$, while for $\Psi_{A,F}$ is the opposite, as indicated by P-values equal to $P_{CGF} = 0.071$ compared to a $P_{Rf} = 0.557$. When *CGF* is set to 22.5 sccm, it leads to the lowest values of Ψ, validating the previous visual observations. This suggests that in a restricted window (as the focused one) *Rf* exerts a minimal impact on Ψ_A. The interaction plots for $\Psi_{A,S}$ and $\Psi_{A,F}$, indeed confirm the significant values of *Rf (*for the first case) and of *CGF* (for the second one), see **Figures 5g** and **5h**.

Figures 6a and **6b** show SEM images of a not favourable print condition which generate bumps across the pillar surface ($n = 50$) and an array of printed PEDOT:PSS composite

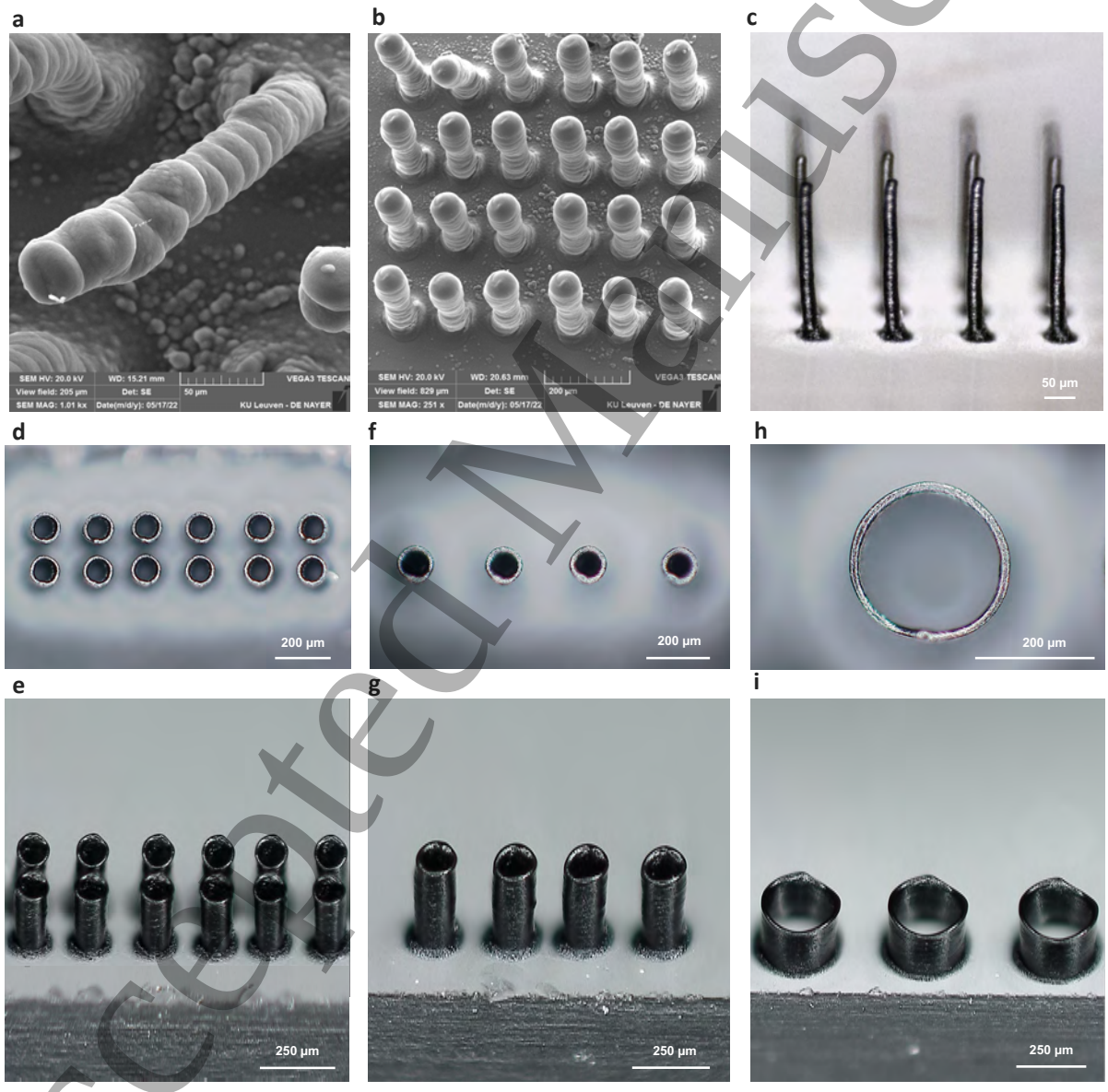

Figure 6. Images of PEDOT:PSS composite pillars. SEM images of (a) a not favourable condition and (b) the best print condition after annealing of micropillars arrays (6 x 4); optical images of (c) a micropillar array at the best condition; top and lateral views of hollowed micropillars with an increasing pillar diameter Ø of (d-e) 100 µm, (f-g) 150 µm, and (h-i) 300 µm.

micropillars (n = 15) at the best condition (N), respectively. **Figure 6c** reports an optical image of a similar micropillar array printed at the condition N at n = 50. By narrowing the print process tuning, it was possible to produce both dense and compact micropillars as well as hollowed ones by increasing the pillar diameter. **Figures 6d-e** display top and lateral views of multiple AJ® printed pillars with diameters of $Ø$ = 100 µm, while **Figures 6f-g** and **6h-i** show views for diameters of $Ø$ = 150 µm and $Ø$ = 300 µm, respectively. These results highlight the AJ®P process's capability to obtain more complex structures, which can be particularly advantageous in bioelectronics applications, such as drug delivery (hollowed cylinders) or cellular interfaces (dense pillars).

3.3 PEDOT:PSS composite micropillars performances

Mechanical performances of PEDOT:PSS composite micropillars, at an average height equal to h = 305.3 ± 30 µm ($Φ$ = 50 µm, n = 30), were evaluated, as reported in **Figures 7a-c**. The micrographs illustrate an elastic behaviour, indicating that the pillars do not reach the fracture point. Instead, they bend under the applied load and then nearly return to their original positions after the test (**Figure 7c**). Stress-strain curve in **Figure 7m** reports that pillars exhibit a compression secant modulus of roughly E = 9.33 ± 1.8 MPa, in the assumption of an ideal cylindrical shape and same contact area for each pillar in the 4x4 array. To test the PEDOT:PSS composite biocompatibility, two cellular lineages, HFs and hiPSCs-derived NSCs, were selected. Immunofluorescence images (**Figures 7d-e** for HFs and **Figures 7f-g** for NSCs, respectively) indicate that both cell lineages can adhere on the surface covered by the PEDOT:PSS composite, however only NSCs exhibit good adhesion, proliferation, and morphology similar to the plastic control, confirming a fully healthy cellular state.

Conversely, HFs on the PEDOT:PSS composite has a reduced confluence and shows a less organised distribution. This difference can be caused by the Matrigel-coating applied on PEDOT:PSS composite for NSCs adhesion that prevents the direct contact NSCs-PEDOT:PSS composite. While this coating mediates biocompatibility rather than the ink itself, it demonstrates that the material can be safely used in bioelectronic applications when paired with a supportive surface layer. No difference in the NSC morphology is detected in the micrographs at 24h between the controls and the induced medium using the PEDOT:PSS composite (**Figures 7h** and **7i**), while clumps of cells are instead visible at 120 h (**Figures 7j** and **7k**).

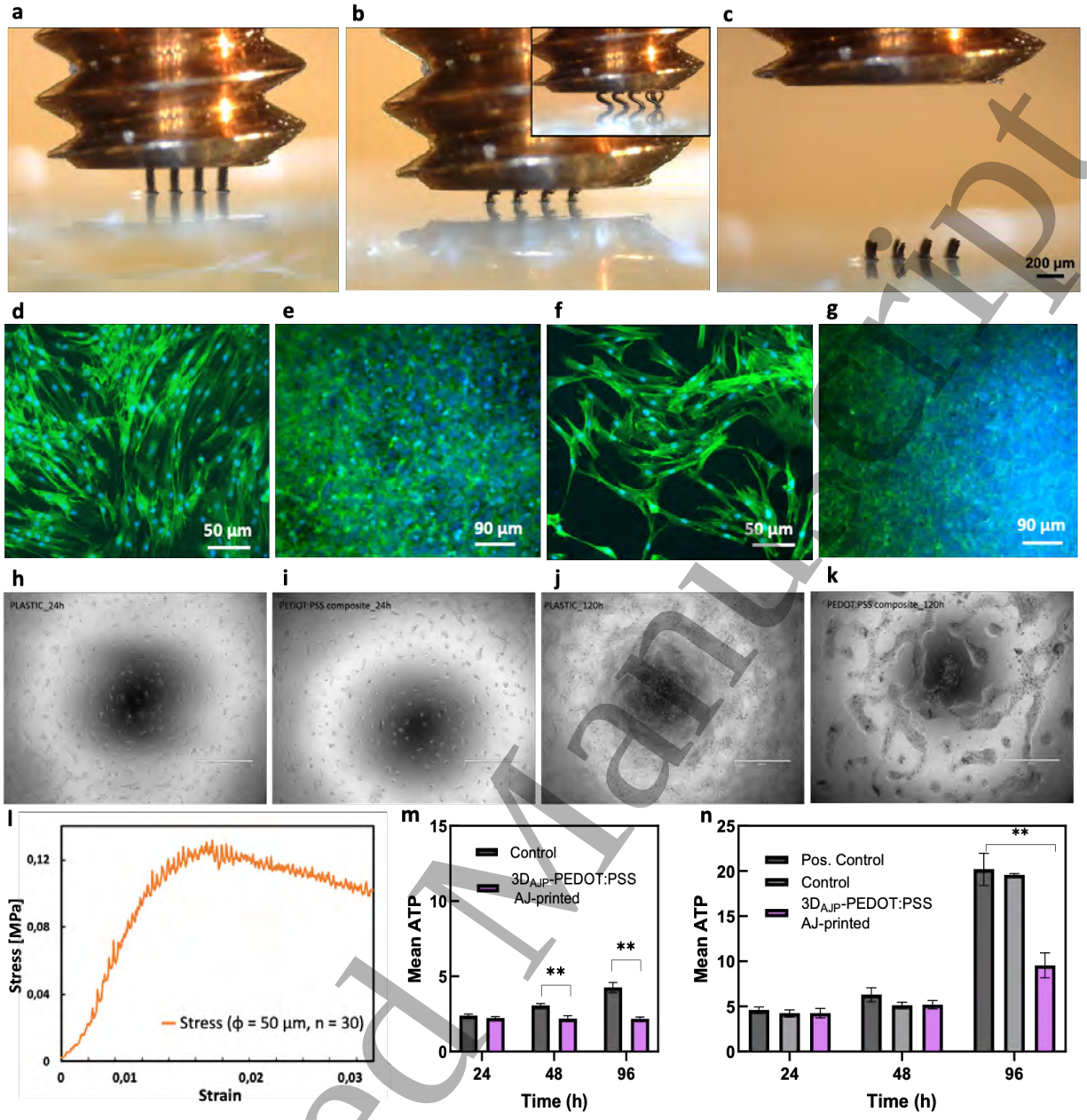

Figure 7. Mechanical performance and application of micropillars at different cellular lineages. Photograms of PEDOT:PSS composite micropillar arrays (a) before, (b) during, and (c) after micro compression test. Fluorescent microscopy images (10x) at day 2 of (d) HFs and (e) human NSCs cultured on plastic control, and (f) HFs and (g) human NSCs cultured on AJ® printed and cured PEDOT:PSS composite ink (N =3). Optical microscopy images of NSCs cultures at 24 h on (h) the control samples and on (i) the AJ® printed PEDOT:PSS composite ink, at 120 h on (j) the control samples and on (k) the AJ® printed PEDOT:PSS composite ink, using an indirect ATP assay. Scale bar 1000 µm; (l) Compression stress-strain curve PEDOT:PSS composite micropillars (N = 3, subsample of 4 pillars for polymeric ink). Cell viability ATP (µM) assays of human NSCs on control and PEDOT:PSS composite printed samples at three time points (24 h, 48 h and 96 h): (m) direct and (n) indirect assay, (N = 3).

Therefore, to better investigate the biocompatibility of the ink, NSCs viability was further evaluated by measuring the amount of ATP metabolic concentration in µM at 24, 48, and 96 h. Direct ATP viability tests of NSCs, seeded at 6×10^4 cells cm^{-2} on the ink coated with Matrigel, demonstrate a constant viability at 24 and 48h, which however is still 50% lower than

the control at 96h (**Figure 7m**). This reduction after 4 days may be due to degradation and thinning of the Matrigel-coating and to the consequent direct exposition of NSCs to ink which may induce a low cellular adhesion, hence less proliferation. Indirect assays confirm that NSCs viability at 96 h is 55% less than the plastic control (**Figure 7n**) and highlight that the reduce cell viability at 96h is not caused by adhesion problem but to ink compounds released in the medium that can perturb the physiological cellular proliferation. Overall, the NSCs viability has still positively increased throughout the entire time; since the NSCs lineage is very delicate, the variation between the samples and the control is still considered a superior result, especially for a bioink developed for bioelectronic applications. Notably, our previous studies have shown that a standard commercial conductive PEDOT:PSS ink can exhibit substantial cytotoxicity even at nanometer-thick coatings, leading to cell death within 24 hours.[32] While the observed biocompatibility of the current composite is mediated by the Matrigel coating and leaves room for further optimization of the ink itself, these results nonetheless represent a marked improvement and highlight the material's great potential for bioelectronic applications.

4. Discussion

A bioconductive ink was developed using a commercial PEDOT:PSS solution as the base component. However, achieving high AR micropillar structures using only PEDOT:PSS is typically highly challenging due to its low solid content and limited mechanical stability. Although such geometries are desirable for enhancing electrical interface performance and promoting tissue integration, they frequently exhibit poor print fidelity, structural instability, and collapse either during or after fabrication, particularly when produced using AM techniques.[9]

Therefore, the proposed formulation leverages the synergistic effects of adding two polyethylene glycols, PEG and EG, which act as conductivity-enhancing agents, and CMC, which functions as a binder to improve the electrochemical stability and stability of the ink. PEG also acts as main ink solid content. The colloidal dispersion is considered stable due to the presence of a good negatively charged electrostatic repulsion, being the zeta potential (ZP) equal to -70.73 ± 14.9 mV of the fresh ink, and to -86.77 ± 4.3 mV of the 1-month-old ink, respectively. The particle diameter of the final PEDOT:PSS composite is equal to 33.28 ± 10.6 µm with a PDI 43.87%. PEDOT:PSS usually has a standard particle size < 15 nm,[58,59] however, the co-solvents molecular structures affect the CP morphology, by expanding the space between PEDOT and PSS chains. It is also observed a particle agglomeration, with an increase of PDI more than 40 %, according to the ISO 22412:2017.[60] Therefore, the apparent mean

hydrodynamic diameter of >15 µm observed in DLS reflects the presence of reversible aggregates. During AJ®P, ultrasonic atomization is assumed to disrupt these aggregates, leading to droplets containing well-dispersed PEDOT:PSS colloids < 500 nm in size,[61] being this upper limit a main constraint in the AJ®P ultrasonic atomization mode. An increase in particle size does not indeed affect the ink processability, as it can undergo successful ultrasonic atomization (**Figure 2d**). This was further verified by the absence of nozzle clogging, the stable printing process, and the reproducible electrical performance obtained.

Regarding conductivity, our ink formulation shows a good value (σ = 495.3 ± 93.1 $S \cdot cm^{-1}$), which is notably higher than most PEDOT:PSS formulations reported for bioelectronics. Higher conductivities have been achieved through aggressive post-treatments, for example, studies reported 1325 S/cm after repeated treatments with hexafluoroacetone (HFA), while the highest value to date, ~4380 S/cm, was obtained via sulfuric acid (H_2SO_4) treatment that induces PEDOT:PSS nanofibril crystallization by PSS removal.[62] However, such approaches remain unsuitable for bioelectronic applications due to the cytotoxic or corrosive nature of the chemicals involved.[50]

The addition of EG was also necessary as a humectant to prevent drying printing during the in-flight jet phase of the AJ®P process. An AJ®P ink must indeed maintain a proper balance between the co-solvent system. An imbalance can lead to suboptimal printing outcomes: a wet ink results in planar 2D deposition without the desired 3D microstructuring, while a dry ink produces brittle and fragmented structures. As illustrated in **Figure 2f**, it is indeed visible the presence of a drying-out effect caused by the fast co-solvent evaporation during the in-flight jet phase and the ink deposition on the substrate. The platen temperature was here set at T = 80°C to allow for in-situ evaporation and pre-sintering of the deposited ink. This phenomenon is especially notable when using the ink formulation which solely contains PEDOT:PSS and PEG. The aerosol jet impacts on the substrate and becomes excessively dried due to the absence of humectants, eventually, generating tree shape-like crystalline structures. The effect is reduced, though still partially visible, when CMC is introduced as a binding agent. When EG is also added, functioning as humectant, no observable crystalline structures are present around the micropillars. Therefore, the inclusion of EG in this formulation played a key role in mitigating dry printing conditions.[40]

The CV profile shown in **Figure 3c** is characteristic of an ideal electric double-layer capacitor (EDLC) response and implies effective ion transport within the polymer matrix. At higher scan rates (150 and 250 mV/s), the CV curves broaden slightly, yet they maintain the overall capacitive shape.[47] This broadening may reflect kinetic limitations associated with ion

transport at elevated scan speeds, but the retention of the capacitive profile suggests that the composite still supports rapid charge/discharge cycles, an essential property for high-frequency applications. It is also notable in **Figure 3d** a decrease value in C_{sp} as the scan rate increases from 57.01 F/g at 20 mV/s to 47.26 F/g at 250 mV/s. This reduction in *Csp* with increasing scan rate is commonly observed in electrochemical capacitors and can be attributed to the insufficient time available for complete ion diffusion and electrochemical interaction within the electrode at higher scan rates. Such behaviour confirms the diffusion-controlled nature of the charge storage process and highlights the importance of optimizing the printing process to maintain performance at fast operating conditions.

As previously reported by the authors, key guidelines for transitioning from 2D to 3D AJ®P require a control over three main print parameters: platen temperature $T \geq 40$°C to initiate a pre-sintering or -annealing process, focusing ratio $Rf \leq 4$ to obtain a focused aerosol jet, and print speed $s \geq 0.4$ mm/s to control the deposition of the ink flow.[30] In this case a platen temperature of $T = 80$°C was chosen to initiate an evaporation on the main solvent, water-based, facilitating the building up of a 3D structure. A lower platen temperature would not have achieved a rapid evaporation, resulting in ink spluttering and only 2D AJ®P. Printing irregularities as shown in **Figure 4a** in condition C, F and I may be attributed to a less controlled and non-uniform material deposition between the printed layers, caused by a rapid evaporation of the ink co-solvents during the in-flight jet phase. This phenomenon is associated with an imbalance between the aerosol deposition and beam focusing, where the amounts of *CGF* and *SGF* play crucial roles, respectively. The lack of such equilibrium indeed leads to the formation of irregular structures. In the case of condition F, this variability is instead attributed to the substantial amount of *CGF* = 30 sccm used in the printing process, for which the *SGF* is insufficient for a precise control of the jet deposition. Therefore, the use of low values of *CGF* and *SGF*, results in the best results, as demonstrated by the best practice condition N, characterized by a *Rf* = 1.2 and a *CGF* = 22.5 sccm. However, it has to be considered that a deviation from the CAD design should be always expected, primarily due to process irregularities and the printer system used, designed for 2D applications, and not especifically for 3D micro-structuring. Surface irregularities in the printed micropillars are also accounted for through the evaluation of the LER sub-index, included in the calculation of Ψ (Supporting Information, **Table S1.1** and **Figure S3**). LER was found to be dependent on the printing parameters. As shown in **Figure 4b**, the optimized combination of *CGF* and *Rf* (thus *SGF*) led to pillars with reduced roughness compared to those in **Figure 4a**, indicating that right parameter selection can mitigate surface irregularities.

The mechanical properties obtained for the AJ® printed micropillars validates their potential as flexible neural micro-interfaces, having an elastic modulus in the range of to the one of polydimethylsiloxane (PDMS), equal E = to 2.5 x 10^6 Pa.[63] Moreover, given that the applied load force is supposed to be greater than the one required for insertion into nerve or brain tissue (Young's Modulus between 2.2 to 3.0 kPa in an adult brain,[64]) these micropillars can potentially be utilized also for in vivo neural interfaces. Saleh et al.,[65] indeed reported that the peak force required to insert a micropillar into an agarose gel that simulates brain stiffness was approximately 0.2-0.4 mN. This value is significantly lower than the minimum force applied to the micropillars in our study.

A critical consideration for the use of these printed PEDOT:PSS composite micropillars as bioelectronic interfaces is their biocompatibility. While PEDOT:PSS offers inherent conductivity and moderate flexibility, its brittleness and potential cytotoxicity at high concentrations necessitate blending with biocompatible and flexible materials, like PEG, and their effective miscibility. However, such modifications must be carefully balanced to preserve both printability and biocompatibility in achieving stable, high-resolution HAR structures suitable for long-term biological interfacing. It is worth noting that, although the biocompatibility is not comparable to the plastic control, as reported in **Figures 7i** and **7j**, it can still be considered acceptable for bioelectronic applications, where the proportion of ink in direct contact with cells is minimal and further diluted in the culture medium.

Therefore,, this work presents a novel PEDOT:PSS-based composite that overcomes the limitations of conventional PEDOT:PSS inks, which are typically restricted to thin films or porous scaffolds. The ink has strong potential for use in micro–AM bioelectronics as 2D or 3D electrode for recording electrophysiological action potentials in tissue engineering. The tunable height and diameter achievable with this AM approach provide precise control over geometry, allowing the production of periodic arrays tailored to probe specific spatial domains *in vitro*.[66] In addition, the resulting 3D micropillar arrays, characterized by mechanical flexibility and electrochemical stability, could be optimized for multiple recording or sensing cycles without significant performance degradation. The ink can be also suitable as an electrode material in biosensors, including electrochemical and impedance-based systems, where long-term electrochemical stability is critical for reliable signal acquisition.[63,67] Like standard PEDOT:PSS formulations, it may be applied as a coating for metal-based electrodes to enhance their electrochemical charge capabilities.[68] In addition, its good electrochemical stability is expected to improve recording performance.[69] Importantly, the demonstrated good biocompatibility with patient-derived hiPSC-derived NSCs suggests that the composite is likely

to be well tolerated by other cell lineages, while maintaining its inherent stability. It is also worth to notice that the structures produced with this ink, especially at high ARs, can be optimized and fully bioelectronically characterized to be potentially integrated in commercial MEAs used in 3D cultures involving cerebral organoids and spheroids. Beyond tissue engineering applications, the ink may also be leveraged in energy storage and thermoelectric devices,[62] where 3D micropillar array architectures provide increased surface area-to-volume ratios, enhancing thermal–electrical conversion efficiency, while simultaneously retaining the composite's inherent biocompatibility and long-term environmental stability.[70,71]

5. Conclusions and Future Perspectives

Bioconductive microarchitectures, as micropillars, microgrooves, microchannels and lattice structures, are becoming fundamental units in bioelectronics, as tissue-electrode interfaces which significantly enhance the interaction between electronic devices and biological tissues due to high surface area and high signal-to-noise ratio. Their improved electrical contact indeed allows a reductio in the electrochemical impedance and facilitates efficient signal transmission. Moreover, their microscale geometry minimizes invasiveness and inflammation and improves attachment and adhesion to irregular surfaces of biological tissues. Finally, their superior biocompatibility permits a long-term tissue-electrode contact, without the presence of cytotoxic elements which can impact on the healthy state of the cellular unit or tissue under investigation. These features are especially critical for advanced applications, such as neurostimulation, electrophysiological recording, tissue engineered scaffolds, and 3D biosensors. Thus, the importance of achieving a controlled, versatile, precise and reliable production of such microarchitectures is fundamental and critical.

In this manuscript, we propose the development and process optimization of a PEDOT:PSS composite that meets all the criteria for bioconductivity and is suitable for processing through thin film formation, 2D deposition, and 3D printing. The ink proposed consists of a PEDOT:PSS aqueous dispersion, with a solid co-binding of biocompatible compounds as PEG, CMC, and EG. PEG was added as a secondary dopant to enhance the conductivity of pristine PEDOT:PSS, CMC was included as a stabilizing polymer to provide structural support, and EG was incorporated to further improve both the conductivity and processability of the ink. The PEDOT:PSS composite ink shows a conductivity up to $\sigma = 495.3 \pm 93.1$ S·cm^{-1}, a good electrochemical stability across multiple scan frequencies over 20 cycles, and superior biocompatibility with hFs and hiPSC-derived NSCs. Particularly, the biocompatibility assessment presented is intended as a preliminary validation to confirm the

suitability of the ink formulation for future bioelectronic integration, with subsequent functional testing and biological system integration planned to fully demonstrate its applicability.

The ink formulated was optimized for the AJ®P technology, since the ink viscosity equal to μ = 7.93 mPa·s at T = 20 °C was ideal for the AJ®P ultrasonic mode, requiring dispersions with viscosities from 1 to 10 mPa·s. The inclusion of EG as a humectant was particularly required for this 3D printing technique to obtain structures with low LER, since it prevented the sporadic formation of crystallized structures, typically caused by the rapid drying of co-solvents during the in-flight aerosol jetting. AJ®P was selected for this study due to the growing interest over the past years in its potential not only for 2D thin film deposition of electronic circuitry but also as a μAM technique for fabricating 3D conductive microarchitectures, such as micropillar arrays and microlattice structures. The AJ®P process parameters were here optimized in combination with the developed ink to enable effective rapid fabrication of micropillars arrays, without the need of masks or binders. A print plate temperature of T = 80 °C was required to enable the formation of 3D microstructures, together with the significant influence of carrier gas flow (*CGF*) and focusing ratio (*Rf*) in achieving fully dense micropillar arrays with high shape fidelity. Arrays of 6 × 4 micropillars were fabricated in under 10 minutes, with an interlayer drying time of approximately 15 seconds per micropillar to allow for co-solvent evaporation. The best print parameters combination was obtained with *CGF* = 22.5 sccm, *SGF* = 27 sccm, s = 0.4 mm/s, and T = 80 °C (Ψ = 0.17). Final pillars showed a height of $h \sim 280$ μm, a diameter of $\Phi \sim 34$ μm, an AR = 8.2, and a bending angle of α = 1.49 rads. This is the highest AR reached in the AJ®P of polymeric pillars at a microscale resolution.[58] Hollowed pillars were further fabricated with varying diameters, demonstrating the versatility of the 3D AJ®P technique in producing both dense and hollow periodic microarrays and microstructures. The pillars also showed flexible behaviour under micro-compression, with a secant compression modulus of approximately 9.33 × 10^6 Pa, making them good for flexible interfaces and highlighting their potential for bioelectronics. Future research will focus on characterizing these microstructures to evaluate their potential for *in vitro* bioelectronic interfaces.

Acknowledgements

Research Foundation Flanders (FWO) is acknowledged for financial support to Miriam Seiti (PhD fellowship N. 1SB1122N). The authors would like to thank Prof. Elisabetta Ceretti and

Prof. Paola Serena Ginestra (TecMec Group, University of Brescia, IT) for their general supervision of the research project.

The authors thank from KU Leuven: Loren De Vogelaer and Akash Verma (AML Lab) for technical assistance, Prof. Raf Dewil and Dr. Sofie Houtmeyers for the use of the FTIR instrument, Prof. Irene Taurino and Dr. Nurul Izni Rusli for the use of CV instruments, Prof. Francisco Molina Lopez for Raman Spectroscopy, Dr. Mohit Sharma (ESAT, Stadius) for fruitful discussions on data analysis, and Eng. Thomas Louwagie at FIBEr (KU Leuven, BE) for supervising the micro-compression tests. The authors also acknowledge MICS (Made in Italy – Circular and Sustainable) Extended Partnership (Next Generation EU (Italian PNRR – M4 C2, 1.3–D.D.1551.11-10-2022, PE00000004 CUP D73C22001250001).

Conflict of interest

The authors declare no conflict of interest.

Received: ((will be filled in by the editorial staff))
Revised: ((will be filled in by the editorial staff))
Published online: ((will be filled in by the editorial staff))

References

[1] A. Tanwar, H. A. Gandhi, D. Kushwaha, J. Bhattacharya, *Materials Today Chemistry* **2022**, *26*, 101153.
[2] Y. Shan, X. Cui, X. Chen, Z. Li, *WIREs Nanomedicine and Nanobiotechnology* **2023**, *15*, e01827.
[3] J. S. Choi, H. J. Lee, S. Rajaraman, D. H. Kim, *Biosensors and Bioelectronics* **2021**, *171*, 112687.
[4] G. Tullii, F. Giona, F. Lodola, S. Bonfadini, C. Bossio, S. Varo, A. Desii, L. Criante, C. Sala, M. Pasini, C. Verpelli, F. Galeotti, M. R. Antognazza, *ACS Appl. Mater. Interfaces* **2019**, *11*, 28125.
[5] Y. Qiu, X. Wang, H. Yu, Y. Zhang, J. Zheng, J. Wang, Q. Gan, L. Liu, W. J. Li, *Additive Manufacturing* **2024**, *88*, 104249.
[6] K. Yang, H. Jung, H.-R. Lee, J. S. Lee, S. R. Kim, K. Y. Song, E. Cheong, J. Bang, S. G. Im, S.-W. Cho, *ACS Nano* **2014**, *8*, 7809.
[7] Y. Lin, R. Yang, X. Wu, *RSC Appl. Polym.* **2023**, *1*, 132.
[8] M. Seiti, P. S. Ginestra, A. Verma, E. Ceretti, E. Ferraris, *Procedia CIRP* **2022**, *110*, 174.
[9] K. Suganuma, *Introduction to Printed Electronics*, **2014**.
[10] S. Zips, B. Huang, S. Hotte, L. Hiendlmeier, C. Wang, K. Rajamani, O. Buriez, G. A. Boustani, Y. Chen, B. Wolfrum, A. Yamada, *ACS Applied Materials and Interfaces* **2023**, *15*, 35950.
[11] N. A. Avra Kundu Madison Royse, Yuen Yee Li Sip, Mikaeel Young, Swadeshmukul Santra, I. L. Z. and Swaminathan Rajaraman Member, **n.d.**
[12] H. Wijshoff, *Current Opinion in Colloid & Interface Science* **2018**, *36*, 20.

[13] A. Bastola, Y. He, J. Im, G. Rivers, F. Wang, R. Worsley, J. S. Austin, O. Nelson-Dummett, R. D. Wildman, R. Hague, C. J. Tuck, L. Turyanska, *Materials Today Electronics* **2023**, *6*, 100058.
[14] Y. Khan, F. J. Pavinatto, M. C. Lin, A. Liao, S. L. Swisher, K. Mann, V. Subramanian, M. M. Maharbiz, A. C. Arias, *Advanced Functional Materials* **2016**, *26*, 1004.
[15] J. Schnitker, N. Adly, S. Seyock, B. Bachmann, A. Yakushenko, B. Wolfrum, A. Offenhäusser, *Advanced Biosystems* **2018**, *2*, 1700136.
[16] M. Magliulo, M. Y. Mulla, M. Singh, E. Macchia, A. Tiwari, L. Torsi, K. Manoli, *Journal of Materials Chemistry C* **2015**, *3*, 12347.
[17] R. Y. Tay, Y. Song, D. R. Yao, W. Gao, *Materials Today* **2023**, *71*, 135.
[18] N. Zavanelli, W.-H. Yeo, *ACS Omega* **2021**, *6*, 9344.
[19] C. Medina-Plaza, C. García-Hernández, J. A. de Saja, J. A. Fernández-Escudero, E. Barajas, G. Medrano, C. García-Cabezón, F. Martin-Pedrosa, M. L. Rodriguez-Mendez, *LWT - Food Science and Technology* **2015**, *62*, 940.
[20] R. Nagata, K. Yokoyama, S. A. Clark, I. Karube, *Biosensors and Bioelectronics* **1995**, *10*, 261.
[21] A. Yakoh, W. Siangproh, O. Chailapakul, N. Ngamrojanavanich, *ACS Appl. Mater. Interfaces* **2020**, *12*, 22543.
[22] Inc. Optomec, **2017**, *M*, 4.
[23] J. Machiels, A. Verma, R. Appeltans, M. Buntinx, E. Ferraris, W. Deferme, *Procedia CIRP* **2021**, *96*, 115.
[24] N. J. Wilkinson, M. A. A. Smith, R. W. Kay, R. A. Harris, *The International Journal of Advanced Manufacturing Technology* **2019**, 1.
[25] S. Agarwala, G. L. Goh, T. S. Dinh Le, J. An, Z. K. Peh, W. Y. Yeong, Y. J. Kim, *ACS Sensors* **2019**, *4*, 218.
[26] A. Verma, R. Goos, J. De Weerdt, P. Pelgrims, E. Ferraris, *Sensors (Basel, Switzerland)* **2022**, *22*, DOI 10.3390/S22197531.
[27] M. S. Saleh, C. Hu, R. Panat, *Science Advances* **2017**, *3*, e1601986.
[28] X. Chen, J. M. Lawrence, L. Wey, L. Schertel, Q. Jing, S. Vignolini, C. Howe, S. Kar-Narayan, J. Z. Zhang, **n.d.**
[29] M. Seiti, P. S. Ginestra, E. Ferraris, *Lecture Notes in Mechanical Engineering* **2024**, *Part F1351*, 19.
[30] M. Seiti, O. Degryse, R. M. Ferraro, S. Giliani, V. Bloemen, E. Ferraris, *International Journal of Bioprinting* **2023**, *9*, 57.
[31] M. Seiti, A. Giuri, C. E. Corcione, E. Ferraris, *Biomaterials advances* **2023**, *154*, DOI 10.1016/J.BIOADV.2023.213655.
[32] M. Seiti, P. S. Ginestra, R. M. Ferraro, S. Giliani, R. M. Vetrano, E. Ceretti, E. Ferraris, *Int J Bioprint* **2022**, *8*, 504.
[33] E. Tomaskovic-Crook, Q. Gu, S. N. A. Rahim, G. G. Wallace, J. M. Crook, *Cells* **2020**, *9*, 658.
[34] L. Groenendaal, F. Jonas, D. Freitag, H. Pielartzik, J. R. Reynolds, *Advanced Materials* **2000**, *12*, 481.
[35] G. Huseynova, Y. H. Kim, J. H. Lee, J. Lee, *Journal of Information Display* **2020**, *21*, 71.
[36] S. R. Muppalla, S. R. Kanatt, S. P. Chawla, A. Sharma, *Food Packaging and Shelf Life* **2014**, *2*, 51.
[37] J. W. Han, A. Prameswati, S. A. N. Entifar, J. H. Kim, A. F. Wibowo, J. Park, J. Lee, S. Kim, D. C. Lim, M. W. Moon, M. S. Kim, Y. H. Kim, *Electronic Materials Letters* **2022**, *18*, 532.
[38] S. Zips, L. Grob, P. Rinklin, K. Terkan, N. Y. Adly, L. J. K. Weiß, D. Mayer, B. Wolfrum, *ACS Appl. Mater. Interfaces* **2019**, *11*, 32778.

[39] P. Zhang, N. Aydemir, M. Alkaisi, D. E. Williams, J. Travas-Sejdic, *ACS Appl. Mater. Interfaces* **2018**, *10*, 11888.
[40] Y. Liu, A. F. McGuire, H.-Y. Lou, T. L. Li, J. B.-H. Tok, B. Cui, Z. Bao, *Proceedings of the National Academy of Sciences* **2018**, *115*, 11718.
[41] Q. Wu, P. Zhang, G. O'Leary, Y. Zhao, Y. Xu, N. Rafatian, S. Okhovatian, S. Landau, T. A. Valiante, J. Travas-Sejdic, M. Radisic, *Biofabrication* **2023**, *15*, 035023.
[42] A. Lunghi, M. Bianchi, P. Greco, R. Viaro, M. Di Lauro, L. Fadiga, F. Biscarini, *Advanced Materials Interfaces* **2025**, *12*, 2500051.
[43] A. Ruggiero, V. Criscuolo, S. Grasselli, U. Bruno, C. Ausilio, C. L. Bovio, O. Bettucci, F. Santoro, *Chem. Commun.* **2022**, *58*, 9790.
[44] M. Seiti, A. Verma, O. Degryse, M. R. Vetrano, E. Ferraris, *Smart Multifunctional Nano-inks: Fundamentals and Emerging Applications* **2023**, 75.
[45] O. Degryse, V. Bloemen, E. Ferraris, *Procedia CIRP* **2022**, *110*, 180.
[46] T. Otsuka, T. Kurosawa, K. Seya, *International Congress on Acoustics* **1980**, *6*, DOI 10.1121/1.1909020.
[47] E. Ceretti, M. Sharma, E. Ferraris, P. S. Ginestra, M. Seiti, *CIRP Annals* **2025**, DOI 10.1016/j.cirp.2025.04.062.
[48] V. Constantoudis, G. P. Patsis, L. H. A. Leunissen, E. Gogolides, *Journal of Vacuum Science & Technology B: Microelectronics and Nanometer Structures Processing, Measurement, and Phenomena* **2004**, *22*, 1974.
[49] R. M. Ferraro, P. S. Ginestra, G. Lanzi, S. Giliani, E. Ceretti, *Procedia CIRP* **2017**, *65*, 225.
[50] M. Seiti, A. Giuri, C. E. Corcione, E. Ferraris, *Biomaterials Advances* **2023**, *154*, 213655.
[51] D. Shao, H. Zhong, L. Zhang, *ChemElectroChem* **2014**, *1*, 1679.
[52] J. Chang, X. Zhang, T. Ge, J. Zhou, *Organic Electronics* **2014**, *15*, 701.
[53] Y. Gourbeyre, E. Guilminot, F. Dalard, *Journal of Materials Science* **2003**, *38*, 1307.
[54] M. Getnet Tadesse, C. Loghin, Y. Chen, L. Wang, D. Catalin, V. Nierstrasz, *Smart Materials and Structures* **2017**, *26*, DOI 10.1088/1361-665X/aa6f25.
[55] Y. Wang, Z. Qu, W. Wang, D. Yu, *Colloids and Surfaces B: Biointerfaces* **2021**, *208*, 112088.
[56] D. Zhao, Q. Zhang, W. Chen, X. Yi, S. Liu, Q. Wang, Y. Liu, J. Li, X. Li, H. Yu, *ACS Applied Materials and Interfaces* **2017**, *9*, 13213.
[57] G. Greco, A. Giuri, S. Bagheri, M. Seiti, O. Degryse, A. Rizzo, C. Mele, E. Ferraris, C. E. Corcione, *Molecules* **2023**, *28*, 2963.
[58] T. Takano, H. Masunaga, A. Fujiwara, H. Okuzaki, T. Sasaki, *Macromolecules* **2012**, *45*, 3859.
[59] H. Yan, S. Arima, Y. Mori, T. Kagata, H. Sato, H. Okuzaki, *Thin Solid Films* **2009**, *517*, 3299.
[60] Y. Takechi-Haraya, T. Ohgita, Y. Demizu, H. Saito, K. ichi Izutsu, K. Sakai-Kato, *AAPS PharmSciTech 2022 23:5* **2022**, *23*, 1.
[61] N. J. Wilkinson, M. A. A. Smith, R. W. Kay, R. A. Harris, *Int J Adv Manuf Technol* **2019**, *105*, 4599.
[62] K. Sun, S. Zhang, P. Li, Y. Xia, X. Zhang, D. Du, F. H. Isikgor, J. Ouyang, *J Mater Sci: Mater Electron* **2015**, *26*, 4438.
[63] Y. Shi, R. Liu, L. He, H. Feng, Y. Li, Z. Li, *Smart Materials in Medicine* **2020**, *1*, 131.
[64] A. Arani, M. C. Murphy, K. J. Glaser, A. Manduca, D. S. Lake, S. A. Kruse, C. R. Jack, R. L. Ehman, J. Huston, **2015**, DOI 10.1016/j.neuroimage.2015.02.016.
[65] M. S. Saleh, S. M. Ritchie, M. A. Nicholas, H. L. Gordon, C. Hu, S. Jahan, B. Yuan, R. Bezbaruah, J. W. Reddy, Z. Ahmed, M. Chamanzar, E. A. Yttri, R. P. Panat, *Science Advances* **2022**, *8*, 4853.

[66] A. Lunghi, A. Mariano, M. Bianchi, N. B. Dinger, M. Murgia, E. Rondanina, A. Toma, P. Greco, M. Di Lauro, F. Santoro, L. Fadiga, F. Biscarini, *Advanced Materials Interfaces* **2022**, *9*, 2200709.
[67] A. Giuri, R. Striani, S. Carallo, S. Colella, A. Rizzo, C. Mele, S. Bagheri, M. Seiti, E. Ferraris, C. E. Corcione, *Electrochimica Acta* **2023**, *441*, 141780.
[68] I. Muguet, A. Maziz, F. Mathieu, L. Mazenq, G. Larrieu, *Advanced Materials* **2023**, *35*, 2302472.
[69] Y. Wen, J. Xu, *Journal of Polymer Science Part A: Polymer Chemistry* **2017**, *55*, 1121.
[70] *Journal of Polymer Materials* **2024**, *40*, 1.
[71] Y. Zhang, H. Zhang, M. Liu, P. Huo, L. Feng, Y. Ren, J. Xu, W. Zhou, T. Xu, *ACS Appl. Mater. Interfaces* **2022**, *14*, 10805.
[72] Y.-G. Park, I. Yun, W. G. Chung, W. Park, D. H. Lee, J.-U. Park, *Advanced Science* **2022**, *9*, 2104623.